NUCLEAR SCIENCE AND ENGINEERING: **166**, 145–166 (2010)

Diffusion Synthetic Acceleration for High-Order Discontinuous Finite Element S_N Transport Schemes and Application to Locally Refined Unstructured Meshes

Yaqi Wang and Jean C. Ragusa*

Texas A&M University, Department of Nuclear Engineering, College Station, Texas 77843

Received July 14, 2009
Accepted February 13, 2010

Abstract—*Diffusion synthetic acceleration (DSA) schemes compatible with adaptive mesh refinement (AMR) grids are derived for the S_N transport equations discretized using high-order discontinuous finite elements. These schemes are directly obtained from the discretized transport equations by assuming a linear dependence in angle of the angular flux along with an exact Fick's law and, therefore, are categorized as partially consistent. These schemes are akin to the symmetric interior penalty technique applied to elliptic problems and are all based on a second-order discontinuous finite element discretization of a diffusion equation (as opposed to a mixed or P_1 formulation). Therefore, they only have the scalar flux as unknowns. A Fourier analysis has been carried out to determine the convergence properties of the three proposed DSA schemes for various cell optical thicknesses and aspect ratios. Out of the three DSA schemes derived, the modified interior penalty (MIP) scheme is stable and effective for realistic problems, even with distorted elements, but loses effectiveness for some highly heterogeneous configurations. The MIP scheme is also symmetric positive definite and can be solved efficiently with a preconditioned conjugate gradient method. Its implementation in an AMR S_N transport code has been performed for both source iteration and GMRes-based transport solves, with polynomial orders up to 4. Numerical results are provided and show good agreement with the Fourier analysis results. Results on AMR grids demonstrate that the cost of DSA can be kept low on locally refined meshes.*

I. INTRODUCTION

In this paper, we consider diffusion synthetic acceleration (DSA) schemes for high-order discontinuous finite element (DFE) spatial discretizations of the S_N transport equation on locally refined unstructured meshes. Progress in the application of adaptive mesh refinement (AMR) techniques to the solution of the S_N transport equation has been reported recently, for instance, in Refs. 1 through 5. However, limited work is available regarding the application of DSA schemes that are compatible with AMR S_N transport solvers. For instance, in Ref. 6, DSA equations are derived for block-AMR S_N transport in the PARTISN code. These DSA equations, differenced using a vertex-centered diffusion discretization that is diamond-like, belong to the family of "partially" consistent schemes; the adapted meshes used are regular subdivisions of meshes in Cartesian xy and rz geometries, hence the denomination of block-AMR. Yet, there is a need to develop AMR-compatible DSA schemes for a wide range of spatial discretizations and geometry types for the S_N transport equation, including discretizations based on DFE. DFE discretizations of the S_N transport equation are well established for unstructured meshes; see, for instance, Ref. 7 for linear DFE on tetrahedral meshes and Refs. 8 and 9 for high-order finite elements on triangular meshes.

For highly diffusive materials (i.e., with scattering ratios $c = \sigma_{s,0}/\sigma_t$ close to 1), the iterative techniques employed to solve the S_N transport equation can be quite ineffective, hence the need to accelerate or precondition these iterations with DSA. Furthermore, it is well established that the spatial discretization of the DSA equations must be "consistent" with the one used for the S_N transport equations to yield unconditionally stable and efficient DSA schemes (Refs. 7 and 10 through 16). To

*E-mail: ragusa@ne.tamu.edu

date, the work by Warsa, Wareing, and Morel[14] regarding a fully consistent DSA scheme for linear discontinuous discretizations on tetrahedra is possibly the only fully consistent example of DSA for general meshes. Their DSA method was derived by using the zeroth and first angular moments of the discretized transport equation, resulting in a mixed-diffusion or P_1 system of equations, with a scalar continuity equation and a first moment vector equation. Even though their scheme achieved full consistency, the overall computational efficiency of their method only outperformed partially consistent schemes under certain circumstances (e.g., for problems that are both highly diffusive and require high angular quadrature order). Alternatively, partially consistent DSA schemes have been motivated by the difficulties associated with the algebraic elimination of the vector unknowns to yield an elliptic diffusion equation. With partially consistent schemes, it is hoped that the reduction in complexity outweighs the degradation in effectiveness. Some partially consistent schemes have been analyzed for unstructured meshes, and results have been reported in Ref. 14: the modified-four-step (M4S) scheme and the Wareing-Larsen-Adams (WLA) scheme. The WLA scheme can be described as a two-stage process: First, a diffusion solution is obtained using a continuous finite element discretization; then a discontinuous update is carried out cell-by-cell in order to provide an appropriate discontinuous scalar flux to the DFE transport solver.

The M4S technique, though effective in one-dimensional slab and two-dimensional (2-D) rectangular geometries, was found to be divergent for three-dimensional (3-D) tetrahedral meshes with linear discontinuous elements. The WLA scheme was found to be a stable and effective DSA technique, though its efficiency degraded as the problems became more optically thick and highly diffusive. However, we note that for the WLA scheme to be used in the context of locally adapted meshes, the continuous diffusion solve must deal with the presence of hanging nodes (i.e., some nodal unknowns are only present on an element and not its neighbor) with the consequence that these unknowns must be constrained in order to keep an approximation that is continuous across elements. Enforcing continuity on adapted meshes can be a nonnegligible task, especially for high-order finite element approximations on unstructured meshes; this has motivated the work presented here, which aims at deriving DSA equations for DFE discretizations on AMR meshes.

In our new approach, we have chosen to derive partially consistent DSA schemes employing a DFE discretization by directly obtaining them from the DFE discretization of the S_N transport equations. Our schemes also belong to the family of partially consistent DSA methods because we only employ the zeroth moment of the DFE transport equation in our derivation and assume that Fick's law is valid in order to eliminate the current unknowns. We show that the resulting DFE discretization for the diffusion equation is remarkably similar to the symmetric interior penalty (IP) stabilization method derived in the mathematics community to solve elliptic (e.g., diffusion) equations using a DFE method.[17] In the mathematical literature, such approximations are also referred to as the discontinuous Galerkin finite element method (DGFEM). Because of the discontinuous nature of the DFE approximation, it is particularly well suited for meshes arising in AMR calculations; i.e., hanging nodes are seamlessly incorporated into the DFE method, and several refinement-level differences between elements can be easily handled. A discontinuous approximation also allows for a straightforward implementation of high-order test functions for AMR meshes, and in this work, we have employed test functions with polynomial orders up to 4.

The outline of the remainder of this paper is as follows. In Sec. II, we recall the standard variational form for the S_N transport equations with DFE discretization. Imposing that the functions in the variational form are linear in angle, along with the assumption of Fick's law, will provide a diffusion variational form derived directly from the discretized S_N equations. We compare the resulting form with the well-known IP diffusion form and propose three DFE DSA schemes to be tested. In Sec. III, we carry out a Fourier analysis of these schemes. In the results of Sec. IV, the most promising DSA schemes are implemented in a 2-D triangular AMR transport code, and the observed convergence properties are compared to our Fourier analysis. Finally, conclusions are provided in Sec. V.

II. WEAK FORMS FOR THE TRANSPORT AND DIFFUSION EQUATIONS

In Sec. II.A, we first give the DFE form of the S_N transport equation. The source iteration (SI) technique, commonly used to obtain a numerical solution to the S_N transport equation, is recalled in Sec. II.B. Next, in Sec. II.C, we derive a DFE weak form for the diffusion equation, starting directly from the DFE weak form of the S_N transport equation. We relate the diffusion form with the standard IP form in Sec. II.D. A modified IP (MIP) form is proposed in Sec. II.E, and the matrix notations for the various forms are given in Sec. II.F, for both the SI technique and the GMRes-based transport solution.

II.A. Discontinuous Finite Element Weak Form for the S_N Transport Equations

Here, we provide the weak form for the S_N transport equations discretized using DFEs. Given an angular quadrature set $\{\vec{\Omega}_m, w_m\}_{1\leq m\leq M}$, the one-group S_N transport equation with isotropic source and scattering is given by

$$(\vec{\Omega}_m\cdot\vec{\nabla}+\sigma_t(\vec{r}))\Psi_m(\vec{r})=\frac{1}{4\pi}\,\sigma_s(\vec{r})\Phi(\vec{r})+\frac{1}{4\pi}\,Q(\vec{r})\ ,$$

$$\text{for } \vec{r}\in\mathcal{D},\ 1\le m\le M\ , \qquad (1)$$

where

$\Psi_m(\vec{r})=\Psi(\vec{r},\vec{\Omega}_m)=$ angular flux at position $\vec{r}$ in direction $\vec{\Omega}_m$

$\sigma_t,\sigma_s=$ total and scattering cross sections, respectively

$\mathcal{D}=$ spatial domain.

The scalar flux is defined and evaluated as follows:

$$\Phi(\vec{r})\equiv\int_{4\pi}\Psi(\vec{r},\vec{\Omega})\,d\Omega\simeq\sum_{m=1}^{M}w_m\Psi_m(\vec{r})\ . \qquad (2)$$

For simplicity, we assume incoming and reflecting boundaries, i.e., $\partial\mathcal{D}=\partial\mathcal{D}^d\cup\partial\mathcal{D}^r$, and the boundary conditions are

$$\Psi_m(\vec{r}_b)=\begin{cases}\Psi_m^{inc}(\vec{r}_b)\ , \\ \qquad \vec{r}_b\in\partial\mathcal{D}_m^{d,-}=\{\partial\mathcal{D}^d \text{ such that } \vec{\Omega}_m\cdot\vec{n}_b<0\} \\ \Psi_{m'}(\vec{r}_b)\ , \\ \qquad \vec{r}_b\in\partial\mathcal{D}_m^{r,-}=\{\partial\mathcal{D}^r \text{ such that } \vec{\Omega}_m\cdot\vec{n}_b<0\}\end{cases}, \qquad (3)$$

where $\vec{n}_b=\vec{n}(\vec{r}_b)$ is the outward unit normal vector at the boundary. The reflecting direction of $\vec{\Omega}_m$ at a point $\vec{r}_b$ on the boundary is given by

$$\vec{\Omega}_{m'}=\vec{\Omega}_m-2(\vec{\Omega}_m\cdot\vec{n}_b)\vec{n}_b\ . \qquad (4)$$

We assume the angular quadrature set satisfies the following two conditions for any outward unit normal vector on the reflecting boundary $\partial\mathcal{D}^r$:

1. $\forall m=1,\ldots,M$; the reflected direction $\vec{\Omega}_{m'}$ is also in the quadrature set.

2. The weights of the incident and reflected directions are equal, i.e., $w_m=w_{m'}$.

A mesh $\mathbb{T}_h$ is used to discretize the domain $\mathcal{D}$ into nonoverlapping linear elements K (specifically triangles in our 2-D application), such that the union of all the elements fully covers $\mathcal{D}$, i.e., $\bigcup_{K\in\mathbb{T}_h}K=\mathcal{D}$. We also assume that the boundary $\partial\mathcal{D}$ consists of straight segments. Next, we give the variational form for the S_N transport equation. This is done by summing the weighted residual obtained for one direction over all directions present in the quadrature set. For completeness, the one-direction residual formula is given in the Appendix and can also be found in the literature; see, for instance, Refs. 7 and 18. Finally, in the context of adaptivity, it is also assumed that the S_N transport equations are solved using the same spatial mesh $\mathbb{T}_h$ for all directions; i.e., AMR meshes are not direction-dependent. As a result, all flux moments are defined and computed on the same mesh. The S_N transport variational form is then as follows:

Find $\Psi_m\in W_{\mathcal{D}}^h$, such that

$$b(\Psi,\Psi^*)=l(\Psi^*)\ ,\quad \forall\Psi_m^*\in W_{\mathcal{D}}^h,\ m=1,\ldots,M\ , \qquad (5)$$

where the bilinear and linear forms are given by

$$b(\Psi,\Psi^*)=a(\Psi,\Psi^*)-\sum_{e\in\partial\mathcal{D}^r}\sum_{\vec{\Omega}_m\cdot\vec{n}_b<0}4\pi w_m\langle\Psi_{m'},\Psi_m^*\rangle_e - (\sigma_s\Phi,\Phi^*)_{\mathcal{D}}\ , \qquad (6)$$

$$a(\Psi,\Psi^*)=\sum_{m=1}^{M}4\pi w_m((\vec{\Omega}_m\cdot\vec{\nabla}+\sigma_t)\Psi_m,\Psi_m^*)_{\mathcal{D}} + \sum_{m=1}^{M}4\pi w_m\langle[\![\Psi_m]\!],\Psi_m^{*+}\rangle_{E_h^i} + \sum_{e\in\partial\mathcal{D}}\sum_{\vec{\Omega}_m\cdot\vec{n}_b<0}4\pi w_m\langle\Psi_m,\Psi_m^*\rangle_e\ , \qquad (7)$$

and

$$l(\Psi^*)=(Q,\Phi^*)_{\mathcal{D}}+\sum_{e\in\partial\mathcal{D}^d}\sum_{\vec{\Omega}_m\cdot\vec{n}_b<0}4\pi w_m\langle\Psi_m^{inc},\Psi_m^*\rangle_e\ . \qquad (8)$$

The bilinear form $a(\cdot,\cdot)$ contains the streaming and interaction terms, as well as the edges' upwind contributions. $a(\cdot,\cdot)$ is the form that is inverted, direction by direction, in a transport sweep. The bilinear form $b(\cdot,\cdot)$ regroups all angular unknowns, the ones from $a(\cdot,\cdot)$ and the scattering and reflective boundary contributions. The form $b(\cdot,\cdot)$ is typically inverted using SI or a Krylov solver. The angular flux, solution to the weak form given by Eq. (5), is the stationary point of a Roussopolos functional.[19] Note that when setting the test functions for all directions except m to zero, we retrieve the one-direction weighted-residual formula, given in the Appendix. In Eq. (5), the finite dimensional polynomial space is $W_{\mathcal{D}}^h=\{\Psi\in L^2(\mathcal{D});\ \Psi|_K\in V_p(K),\ \forall K\in\mathbb{T}_h\}$, where $V_p(K)$ is the space of polynomials of degree up to p on element K; the set of interior edges is $E_h^i=\cup_{K_1,K_2\in\mathbb{T}_h}(\partial K_1\cap\partial K_2)$; the trace of the angular flux on the edges is defined as

$$\Psi_m^{\pm}\equiv\lim_{s\to0^{\pm}}\Psi_m(\vec{r}+s\vec{\Omega}_m)\ ; \qquad (9)$$

and the element and edge integrals are given by

$$(f,g)_K\equiv\int_K fg\,d\vec{r}\ , \qquad (10a)$$

$$\langle f, g\rangle_e \equiv \int_e |\vec{\Omega}_m \cdot \vec{n}_e(\vec{r})| fg \, \mathrm{d}s \ , \tag{10b}$$

$$(f, g)_{\mathcal{D}} \equiv \sum_{K \in \mathbb{T}_h} (f, g)_K \ , \tag{10c}$$

and

$$\langle f, g\rangle_{E_h^i} \equiv \sum_{e \in E_h^i} \langle f, g\rangle_e \ , \tag{10d}$$

where $\vec{n}_e(\vec{r})$ is the unit normal vector for edge e at position $\vec{r}$. The inter-element jump is defined as $[\![\Psi_m]\!] = \Psi_m^+ - \Psi_m^-$.

II.B. Source Iteration

The DFE discretized transport equation of Eq. (5) can be solved using SI. One step of SI can be written as

$$\Phi^{(\ell)} = \sum_{m=1}^{M} w_m \Psi_m^{(\ell)} \tag{11a}$$

and

$$a(\Psi^{(\ell+1/2)}, \Psi^*) = l(\Psi^*) + (\sigma_s \Phi^{(\ell)}, \Phi^*)_{\mathcal{D}} + \sum_{e \in \partial \mathcal{D}^r} \sum_{\vec{\Omega}_m \cdot \vec{n}_b < 0} 4\pi w_m \langle \Psi_{m'}^{(\ell)}, \Psi_m^* \rangle_e \ , \tag{11b}$$

where index ℓ represents the previous iterate and $\ell + \frac{1}{2}$ is the current iterate (the half-integer notation is standard in the context of accelerated transport solves). Note that the above iterative process converges both the scalar flux and the outgoing angular fluxes on the reflecting boundaries; we denote these boundary angular flux unknowns as the significant angular fluxes (SAFs). Note that SAFs can also occur inside the domain, depending on the mesh topology, leading to dependencies or cycles in the graph of the transport sweeps.

Replacing the iterates ℓ and $\ell + \frac{1}{2}$ with the converged solution, Ψ^{cvg} and Φ^{cvg}, we have

$$\Phi^{cvg} = \sum_{m=1}^{M} w_m \Psi_m^{cvg} \tag{12a}$$

and

$$a(\Psi^{cvg}, \Psi^*) = l(\Psi^*) + (\sigma_s \Phi^{cvg}, \Phi^*)_{\mathcal{D}} + \sum_{e \in \partial \mathcal{D}^r} \sum_{\vec{\Omega}_m \cdot \vec{n}_b < 0} 4\pi w_m \langle \Psi_{m'}^{cvg}, \Psi_m^* \rangle_e \ . \tag{12b}$$

Subtracting Eq. (12) and Eq. (11), we obtain the following equations for the iteration error:

$$\mathcal{E}^{(\ell)} = \sum_{m=1}^{M} w_m \epsilon_m^{(\ell)} \tag{13a}$$

and

$$a(\epsilon^{(\ell+1/2)}, \Psi^*) = (\sigma_s \mathcal{E}^{(\ell)}, \Phi^*)_{\mathcal{D}} + \sum_{e \in \partial \mathcal{D}^r} \sum_{\vec{\Omega}_m \cdot \vec{n}_b < 0} 4\pi w_m \langle \epsilon_{m'}^{(\ell)}, \Psi_m^* \rangle_e \ , \tag{13b}$$

where the angular error and the scalar error are, respectively,

$$\epsilon^{(\ell)} = \Psi^{cvg} - \Psi^{(\ell)} \tag{14a}$$

and

$$\mathcal{E}^{(\ell)} = \Phi^{cvg} - \Phi^{(\ell)} \ . \tag{14b}$$

Note that in Eq. (13), the external volumetric source and the incident Dirichlet boundary conditions are no longer present [the linear form $l(\cdot)$ has canceled out]. We now introduce the differences in successive angular and scalar iterates

$$\delta\Psi^{(\ell)} = \Psi^{(\ell+1/2)} - \Psi^{(\ell)} = \epsilon^{(\ell)} - \epsilon^{(\ell+1/2)} \tag{15a}$$

and

$$\delta\Phi^{(\ell)} = \Phi^{(\ell+1/2)} - \Phi^{(\ell)} = \mathcal{E}^{(\ell)} - \mathcal{E}^{(\ell+1/2)} \tag{15b}$$

and can, therefore, obtain an equation for the angular error at iteration $\ell + \frac{1}{2}$:

$$b(\epsilon^{(\ell+1/2)}, \Psi^*) = (\sigma_s \delta\Phi^{(\ell)}, \Phi^*)_{\mathcal{D}} + \sum_{e \in \partial \mathcal{D}^r} \sum_{\vec{\Omega}_m \cdot \vec{n}_b < 0} 4\pi w_m \langle \delta\Psi_{m'}^{(\ell)}, \Psi_m^* \rangle_e \ . \tag{16}$$

In the angular error equation, Eq. (16), the inhomogeneous surface source terms are solely a function of the changes in angular fluxes $\delta\Psi^{(\ell)}$, and the volumetric source terms are due to the changes in the scalar flux $\delta\Phi^{(\ell)}$. Note that Eq. (16) is written in terms of the full transport bilinear form $b(\cdot,\cdot)$ containing the bilinear form $a(\cdot,\cdot)$ as well as the scattering and reflecting boundary terms. Solving Eq. (16) for the exact error $\epsilon^{(\ell+1/2)}$ would yield the exact corrective terms needed to obtain the converged transport solution, i.e.,

$$\Psi^{cvg} = \Psi^{(\ell+1/2)} + \epsilon^{(\ell+1/2)} \tag{17a}$$

and

$$\Phi^{cvg} = \Phi^{(\ell+1/2)} + \mathcal{E}^{(\ell+1/2)} \ . \tag{17b}$$

Unfortunately, Eq. (16) is as difficult to solve as the original transport problem itself, Eq. (5). The concept of synthetic acceleration will be used to derive an approximation to Eq. (16) in order to obtain, at a lesser cost, the corrective terms.

II.C. Derivation of the Discontinuous Finite Element Diffusion Synthetic Acceleration Equations

In this section, we derive an approximate (diffusion) operator in lieu of Eq. (16). The solution of this operator, denoted by a ˜ symbol, will be employed as corrective terms to update the next transport solution:

$$\Psi^{(\ell+1)} = \Psi^{(\ell+1/2)} + \tilde{\epsilon}^{(\ell+1/2)} \tag{18a}$$

and

$$\Phi^{(\ell+1)} = \Phi^{(\ell+1/2)} + \tilde{\mathcal{E}}^{(\ell+1/2)} \ . \tag{18b}$$

First, we restrict the angular dependence of the primal corrective fluxes and the dual test functions by assuming they satisfy a diffusion expansion:

$$\tilde{\epsilon}_m^{(\ell+1/2)} = \frac{1}{4\pi}\left(\phi - 3D\vec{\nabla}\phi\cdot\vec{\Omega}_m\right) \tag{19a}$$

and

$$\tilde{\Psi}_m^* = \frac{1}{4\pi}\left(\phi^* + 3D\vec{\nabla}\phi^*\cdot\vec{\Omega}_m\right) \ ; \tag{19b}$$

i.e., both the primal and dual angular fluxes are linearly anisotropic. The scalar flux ϕ in Eq. (19a) is the scalar corrective term, $\phi = \tilde{\mathcal{E}}^{(\ell+1/2)}$ (this is only a notational convenience). We have employed a P_1 expansion in which we have explicitly used Fick's law to eliminate the first angular moment (the net current) from the P_1 expansion. The primal and dual Fick's laws read as follows:

$$\vec{J} = -D\vec{\nabla}\phi \tag{20a}$$

and

$$\vec{J}^* = D\vec{\nabla}\phi^* \ . \tag{20b}$$

We will later see that the diffusion coefficient D will be obtained naturally and will follow its usual definition. We then substitute these assumed expansions for the primal and test function spaces into the weak form for the DFE S_N transport update equation, Eq. (16), in order to obtain a synthetic DFE diffusion operator in which the scalar flux ϕ is the only unknown. The remainder of the derivation consists in angular integration and algebraic manipulations and is outlined below.

We start the derivation by evaluating the simplest terms in the variational form for the update equation, namely, the discrete angular integral for the total and scattering reaction terms. These algebraic calculations are simple and yield, respectively,

$$\sum_{m=1}^{M} 4\pi w_m(\sigma_t\tilde{\epsilon}_m^{(\ell+1/2)}, \tilde{\Psi}_m^*)_{\mathcal{D}} = (\sigma_t\phi, \phi^*)_{\mathcal{D}} - (3\sigma_t D\vec{\nabla}\phi, D\vec{\nabla}\phi^*)_{\mathcal{D}} \tag{21}$$

and

$$(\sigma_s\tilde{\mathcal{E}}^{(\ell+1/2)}, \tilde{\Phi}^*)_{\mathcal{D}} = (\sigma_s\phi, \phi^*)_{\mathcal{D}} \ , \tag{22}$$

where the following properties of the angular quadrature set have been used:

$$\sum_{m=1}^{M} w_m = 4\pi \ , \tag{23a}$$

$$\sum_{m=1}^{M} w_m\vec{\Omega}_m = 0 \ , \tag{23b}$$

and

$$\sum_{m=1}^{M} w_m\vec{\Omega}_m\vec{\Omega}_m = \frac{4\pi}{3} I \ . \tag{23c}$$

Merging these two reaction terms [Eqs. (21) and (22)] appearing in $b(\cdot,\cdot)$ yields

$$(\sigma_a\phi, \phi^*)_{\mathcal{D}} - (\vec{\nabla}\phi, D\vec{\nabla}\phi^*)_{\mathcal{D}} \ , \tag{24}$$

with the following standard definitions naturally arising in the derivation:

$$D = \frac{1}{3\sigma_t} \tag{25}$$

and

$$\sigma_a = \sigma_t - \sigma_s \ . \tag{26}$$

It is easy to see that with anisotropic scattering, D would have been equal to $1/3\sigma_{tr}$. We now analyze the last volumetric term in $b(\cdot,\cdot)$, i.e., the streaming term:

$$\begin{aligned}\sum_{m=1}^{M} 4\pi w_m(\vec{\Omega}_m\cdot\vec{\nabla}\tilde{\epsilon}_m^{(\ell+1/2)}, \tilde{\Psi}_m^*)_{\mathcal{D}} &= (\vec{\nabla}\phi, D\vec{\nabla}\phi^*)_{\mathcal{D}} - (\vec{\nabla}\cdot D\vec{\nabla}\phi, \phi^*)_{\mathcal{D}} \\ &= (\vec{\nabla}\phi, D\vec{\nabla}\phi^*)_{\mathcal{D}} + (D\vec{\nabla}\phi, \vec{\nabla}\phi^*)_{\mathcal{D}} \\ &\quad + (D\vec{\nabla}\phi^+\cdot\vec{n}_e, \phi^{*,+})_{E_h^i} - (D\vec{\nabla}\phi^-\cdot\vec{n}_e, \phi^{*,-})_{E_h^i} \\ &\quad - (D\vec{\nabla}\phi\cdot\vec{n}_e, \phi^*)_{\partial\mathcal{D}} \ ,\end{aligned} \tag{27}$$

where integration by parts was performed and the following definition for the scalar flux on the edges has been used:

$$\phi^{\pm} = \lim_{s \to 0^{\pm}} \phi(\vec{r} + s\vec{n}_e) \ . \tag{28}$$

Note the difference in the edge definition between the angular fluxes, where the ± superscript depended on the discrete ordinate direction, and the diffusion scalar flux, where there are no specific directions associated with the scalar flux. $\vec{n}_e$ is the normal unit vector associated with a given edge e. The orientation of $\vec{n}_e$ on an interior edge is arbitrary. However, on the boundary edges, this vector needs to be oriented outward. In the derivation of Eq. (27), an additional quadrature property has been utilized:

$$\sum_{m=1}^{M} w_m \vec{\Omega}_m \vec{\Omega}_m \vec{\Omega}_m = 0 \ . \tag{29}$$

Before processing the edge terms appearing in the DFE S_N variational form, we introduce the following edge average and edge jump definitions for the scalar flux on the interior edges (similar definitions for the derivatives of scalar flux on the edges can be inferred from these):

$$[\![\phi]\!] = \phi^{+} - \phi^{-} \tag{30}$$

and

$$\{\!\{\phi\}\!\} = (\phi^{+} + \phi^{-})/2 \ , \tag{31}$$

and we define the edge integral in the context of the diffusion equation as follows:

$$(\phi, \phi^*)_e = \int_e \phi \phi^* \, \mathrm{d}s \ . \tag{32}$$

(Recall that in the context of the transport equation, the edge integral contains a $|\vec{\Omega}_m \cdot \vec{n}_e|$ term.)

Let us now consider the term related to the interior edges:

$$\begin{aligned}
&\sum_{m=1}^{M} 4\pi w_m \langle [\![\tilde{\epsilon}_m^{(\ell+1/2)}]\!], \tilde{\Psi}_m^{*+} \rangle_{E_h^i} \\
&\quad = \sum_{e \in E_h^i} \sum_{m=1}^{M} 4\pi w_m |\vec{\Omega}_m \cdot \vec{n}_e| ([\![\tilde{\epsilon}_m^{(\ell+1/2)}]\!], \tilde{\Psi}_m^{*+})_e \\
&\quad = \sum_{e \in E_h^i} \Bigg[\sum_{\vec{\Omega}_m \cdot \vec{n}_e > 0} \frac{w_m}{4\pi} |\vec{\Omega}_m \cdot \vec{n}_e| ([\![\phi]\!] - 3[\![D\vec{\nabla}\phi]\!] \cdot \vec{\Omega}_m, \phi^{*+} + 3D\vec{\nabla}\phi^{*+} \cdot \vec{\Omega}_m)_e \\
&\qquad - \sum_{\vec{\Omega}_m \cdot \vec{n}_e < 0} \frac{w_m}{4\pi} |\vec{\Omega}_m \cdot \vec{n}_e| ([\![\phi]\!] - 3[\![D\vec{\nabla}\phi]\!] \cdot \vec{\Omega}_m, \phi^{*-} + 3D\vec{\nabla}\phi^{*-} \cdot \vec{\Omega}_m)_e \Bigg] \\
&\quad = \sum_{e \in E_h^i} \sum_{\vec{\Omega}_m \cdot \vec{n}_e > 0} \frac{w_m}{4\pi} |\vec{\Omega}_m \cdot \vec{n}_e| \\
&\qquad [([\![\phi]\!] - 3[\![D\vec{\nabla}\phi]\!] \cdot \vec{\Omega}_m, \phi^{*+} + 3D\vec{\nabla}\phi^{*+} \cdot \vec{\Omega}_m)_e - ([\![\phi]\!] + 3[\![D\vec{\nabla}\phi]\!] \cdot \vec{\Omega}_m, \phi^{*-} - 3D\vec{\nabla}\phi^{*-} \cdot \vec{\Omega}_m)_e] \\
&\quad = \frac{1}{4} ([\![\phi]\!], [\![\phi^*]\!])_{E_h^i} + ([\![\phi]\!], \{\!\{D\vec{\nabla}\phi^* \cdot \vec{n}\}\!\})_{E_h^i} - ([\![D\vec{\nabla}\phi \cdot \vec{n}]\!], \{\!\{\phi^*\}\!\})_{E_h^i} \\
&\qquad - \frac{9}{16} ([\![D\vec{\nabla}\phi]\!], [\![D\vec{\nabla}\phi^*]\!])_{E_h^i} - \frac{9}{16} ([\![D\vec{\nabla}\phi \cdot \vec{n}]\!], [\![D\vec{\nabla}\phi^* \cdot \vec{n}]\!])_{E_h^i} \ ,
\end{aligned} \tag{33}$$

where we employed the following properties of the angular quadrature:

$$\sum_{\vec{\Omega}_m \cdot \vec{n} > 0} w_m |\vec{\Omega}_m \cdot \vec{n}| \approx \pi \ , \tag{34a}$$

$$\sum_{\vec{\Omega}_m \cdot \vec{n} > 0} w_m |\vec{\Omega}_m \cdot \vec{n}| \vec{\Omega}_m \approx \frac{2\pi}{3} \vec{n} \ , \tag{34b}$$

and

$$\sum_{\vec{\Omega}_m\cdot\vec{n}>0} w_m|\vec{\Omega}_m\cdot\vec{n}|\vec{\Omega}_m\vec{\Omega}_m \approx \frac{\pi}{4}(I+\vec{n}\vec{n}) \ . \tag{34c}$$

Although these properties cannot be strictly satisfied, numerical results show that this quadrature effect is negligible for DSA. Note that $\vec{n}\vec{n}$ is a rank-2 tensor. The boundary terms are treated similarly.

Now, putting all terms in Eqs. (24), (27), and (33) together, along with the boundary terms that we omitted for brevity, we obtain the following diffusion variational form for the corrective scalar flux:

$$b_{DCF}(\phi,\phi^*) = l_{DCF}(\phi^*) \ , \tag{35}$$

where the bilinear form is

$$\begin{aligned} b_{DCF}(\phi,\phi^*) = {} & (\sigma_a\phi,\phi^*)_{\mathcal{D}} + (D\vec{\nabla}\phi,\vec{\nabla}\phi^*)_{\mathcal{D}} \\ & + \frac{1}{4}([\![\phi]\!],[\![\phi^*]\!])_{E_h^i} + ([\![\phi]\!],\{\!\{D\partial_n\phi^*\}\!\})_{E_h^i} + (\{\!\{D\partial_n\phi\}\!\},[\![\phi^*]\!])_{E_h^i} \\ & + \frac{1}{4}(\phi,\phi^*)_{\partial\mathcal{D}^d} - \frac{1}{2}(\phi,D\partial_n\phi^*)_{\partial\mathcal{D}^d} - \frac{1}{2}(D\partial_n\phi,\phi)_{\partial\mathcal{D}^d} \\ & - \frac{9}{16}([\![D\vec{\nabla}\phi]\!],[\![D\vec{\nabla}\phi^*]\!])_{E_h^i} - \frac{9}{16}([\![D\partial_n\phi]\!],[\![D\partial_n\phi^*]\!])_{E_h^i} \\ & - \frac{9}{16}(D\vec{\nabla}\phi,D\vec{\nabla}\phi^*)_{\partial\mathcal{D}^d} - \frac{9}{16}(D\partial_n\phi,D\partial_n\phi^*)_{\partial\mathcal{D}^d} \\ & - \frac{9}{4}(D\partial_n\phi,D\partial_n\phi^*)_{\partial\mathcal{D}^r} \ , \end{aligned} \tag{36}$$

and the linear form is

$$\begin{aligned} l_{DCF}(\phi^*) = {} & (Q_0,\phi^*)_{\mathcal{D}} + (J^{inc},\phi^*)_{\partial\mathcal{D}^r} \\ & - (\vec{\Upsilon}^{inc},D\vec{\nabla}\phi^*)_{\partial\mathcal{D}^r} + 2(\vec{\Upsilon}^{inc}\cdot\vec{n},D\partial_n\phi^*)_{\partial\mathcal{D}^r} \ . \end{aligned} \tag{37}$$

Since this variational form was obtained directly from the S_N variational form by (a) assuming a P_1 expansion in the primal and dual functions and (b) assuming Fick's law, we have labeled this form as diffusion conforming form (DCF). When employing the DCF form as a synthetic accelerator for transport, the volumetric term Q_0 and the incoming values J^{inc}, $\vec{\Upsilon}^{inc}$ appearing in Eq. (37) are given by

$$Q_0 = \delta\Phi^{(\ell)} \ , \tag{38}$$

$$J^{inc} = \sum_{\vec{\Omega}_m\cdot\vec{n}_b>0} w_m|\vec{\Omega}_m\cdot\vec{n}_b|\delta\Psi_m^{(\ell)} \ , \tag{39}$$

and

$$\vec{\Upsilon}^{inc} = -\sum_{\vec{\Omega}_m\cdot\vec{n}_b>0} 3w_m\vec{\Omega}_m|\vec{\Omega}_m\cdot\vec{n}_b|\delta\Psi_m^{(\ell)} \ , \tag{40}$$

where Q_0 represents the volumetric source term due to the successive error in the scattering term, J^{inc} is the incoming partial current, and $\vec{\Upsilon}^{inc}$ is the next higher moment due to the difference in two successive angular fluxes on reflective boundaries (the presence of SAFs on reflecting boundaries introduces a nonhomogeneous surface source in the DSA calculations). Again, in the update equation, no contributions are present due to the fixed external source or the Dirichlet boundary conditions.

Finally, we note that the bilinear form of DCF is symmetric but not positive definite and we employ a symmetric quasi-minimal residual (SQMR) method[20] to solve it. Once ϕ is obtained, both the scalar flux and SAF are corrected (accelerated) according to Eqs. (18) and (19a).

II.D. Standard Interior Penalty Form for the Discontinuous Finite Element Diffusion Equations

Now, we recall the symmetric IP DFE discretization for the diffusion equation. The IP formulation is one of the oldest techniques employed to solve the diffusion equation using discontinuous approximations. It was first introduced by Nitsche[21] to weakly enforce Dirichlet

boundary conditions on the domain's boundary. Instead of enforcing that the approximation ϕ be equal to the Dirichlet value ϕ^d at any point on the boundary, Nitsche suggested to enforce the boundary condition in a weak sense, as $\int_{\partial\mathcal{D}}(\phi - \phi^d)^2$. Subsequently, by extending Nitsche's approach to all interior edges (or faces in 3-D), the condition on the continuity of the approximation in between elements can be relaxed and satisfied weakly using $\int_e(\phi^+ - \phi^-)^2$, where e is an interior edge and ϕ^+, ϕ^- are the edge values in the two elements sharing edge e.[22]

Rather than deriving the diffusion update operator from the discretized transport operator (see Sec. II.C), another option to obtain a discontinuous update solution would be to directly apply the IP technique to the following diffusion update equation:

$$-\vec{\nabla}\cdot D\vec{\nabla}\phi + \sigma_a\phi = Q_0 \quad \text{for } \vec{r}\in\mathcal{D}\ , \tag{41}$$

$$\frac{1}{4}\phi - \frac{1}{2}D\partial_n\phi = 0 \quad \text{for } \vec{r}\in\partial\mathcal{D}^d\ , \tag{42}$$

and

$$-D\partial_n\phi = J^{inc} \quad \text{for } \vec{r}\in\partial\mathcal{D}^r\ , \tag{43}$$

where Q_0 denotes, again, the fixed scattering source due to $\sigma_s\delta\Phi^\ell$. The reflective boundary conditions of the transport operator are subjected to a nonhomogeneous Neumann source (a nonhomogeneous Neumann boundary condition holds on the reflective boundary of the original transport problem $\mathcal{D}^r$). The Dirichlet boundary condition of the original transport problem is now a zero-incoming condition, Eq. (42), on $\partial\mathcal{D}^d$.

The IP variational form is given by $b_{IP}(\phi,\phi^*) = l_{IP}(\phi^*)$, where the bilinear and linear forms are (see Ref. 23)

$$\begin{aligned} b_{IP}(\phi,\phi^*) = {} & (\sigma_a\phi,\phi^*)_{\mathcal{D}} + (D\vec{\nabla}\phi,\vec{\nabla}\phi^*)_{\mathcal{D}} \\ & + (\kappa_e^{IP}[\![\phi]\!],[\![\phi^*]\!])_{E_h^i} \\ & + ([\![\phi]\!],\{\!\{D\partial_n\phi^*\}\!\})_{E_h^i} + (\{\!\{D\partial_n\phi\}\!\},[\![\phi^*]\!])_{E_h^i} \\ & + (\kappa_e^{IP}\phi,\phi^*)_{\partial\mathcal{D}^d} - \frac{1}{2}(\phi,D\partial_n\phi^*)_{\partial\mathcal{D}^d} \\ & - \frac{1}{2}(D\partial_n\phi,\phi)_{\partial\mathcal{D}^d} \end{aligned} \tag{44}$$

and

$$l_{IP}(\phi^*) = (Q_0,\phi^*)_{\mathcal{D}} + (J^{inc},\phi^*)_{\partial\mathcal{D}^r}\ . \tag{45}$$

It is well-known that the IP form needs to be stabilized, and the edge stabilization parameter κ_e^{IP} is given by the following formula[24]:

$$\kappa_e^{IP} = \begin{cases} \dfrac{c(p^+)}{2}\dfrac{D^+}{h_\perp^+} + \dfrac{c(p^-)}{2}\dfrac{D^-}{h_\perp^-} \\ \quad \text{on interior edges, i.e., } e\in E_h^i \\ c(p)\dfrac{D}{h_\perp} \\ \quad \text{on boundary edges, i.e., } e\in\partial\mathcal{D}^d\ , \end{cases} \tag{46}$$

where $c(p) = Cp(p+1)$, C is a constant (we used $C = 2$), p is the polynomial order, D is the diffusion coefficient, and $h_\perp$ is the length of the cell in the direction orthogonal to edge e (for triangles, $h_\perp = 2A/L$, where A is the element area and L is the edge length). The $+$ and $-$ symbols represent the values on either side of an edge. With the penalty coefficient κ_e^{IP}, the IP bilinear form is symmetric positive definite (SPD) and is solved using a preconditioned conjugate gradient (CG) technique [with symmetric successive overrelaxation (SSOR) as preconditioner]. When comparing the ad hoc IP form and the DCF form, we note the following differences:

1. Vacuum and reflective boundaries are treated as homogeneous Cauchy and nonhomogeneous Neumann boundary types in the IP diffusion form.

2. In the IP form, the penalty coefficient can vary locally with the local polynomial order and the mesh size, while it is fixed to $\frac{1}{4}$ in the DCF form.

3. In the IP form, there are no derivative edge terms in both the primal and dual functions.

4. The $\vec{\Upsilon}^{inc}$ contribution is absent in the IP form.

II.E. Modified Interior Penalty Form

As will be documented with our Fourier analysis, both the DCF and the IP forms are not unconditionally stable diffusion synthetic accelerators for transport solves. Because of the complexity of the DCF form, our initial efforts concentrated on utilizing the IP form. As will be shown in Sec. III.A, the IP DSA form was found to be unstable for cells with large mean free paths. In these configurations, the IP stabilization parameter tends to zero ($\kappa_e^{IP}\propto\tau^{-1}$, where τ is the optical thickness). To remedy this lack of stabilization in the IP form, the following modification to the penalty coefficient is proposed:

$$\kappa_e = \max\left(\kappa_e^{IP},\frac{1}{4}\right)\ , \tag{47}$$

where the $\frac{1}{4}$ coefficient is borrowed from the DCF derivation. The resulting form is hereafter referred to as the MIP form and reads $b_{MIP}(\phi,\phi^*) = l_{MIP}(\phi^*)$, where the bilinear and linear forms are

$$b_{MIP}(\phi,\phi^*) = (\sigma_a\phi,\phi^*)_{\mathcal{D}} + (D\vec{\nabla}\phi,\vec{\nabla}\phi^*)_{\mathcal{D}} + (\kappa_e[\![\phi]\!],[\![\phi^*]\!])_{E_h^i} + ([\![\phi]\!],\{\!\{D\partial_n\phi^*\}\!\})_{E_h^i} + (\{\!\{D\partial_n\phi\}\!\},[\![\phi^*]\!])_{E_h^i} + (\kappa_e\phi,\phi^*)_{\partial\mathcal{D}^d} - \frac{1}{2}(\phi,D\partial_n\phi^*)_{\partial\mathcal{D}^d} - \frac{1}{2}(D\partial_n\phi,\phi)_{\partial\mathcal{D}^d} \quad (48)$$

and

$$l_{MIP}(\phi^*) = (Q_0,\phi^*)_{\mathcal{D}} + (J^{inc},\phi^*)_{\partial\mathcal{D}^r} \ . \quad (49)$$

The MIP form is SPD. Finally, we have obtained three DFE diffusion forms (DCF, IP, and MIP) as a potential operator for DSA. All of them are symmetric, but only the IP and MIP forms are also positive definite. Note that all these diffusion bilinear and linear forms can be coded as given.

II.F. Matrix Notation

In this section, we provide the matrix notation for the above DSA forms, in both the context of unpreconditioned and preconditioned SI and GMRes iterations.

II.F.1. Unaccelerated Transport Solves

For simplicity, let us first suppose that the graph of the transport sweeps does not possess any cycle; i.e., there are no SAFs. With an appropriate numbering of the angular flux and scalar flux unknowns into vectors $\boldsymbol{\Psi}$ for the angular fluxes and $\boldsymbol{\Phi}$ for the scalar flux, we can represent the transport equation Eq. (1) and the scalar flux equation Eq. (2) in the following matrix form:

$$\mathbf{L}\boldsymbol{\Psi} - \mathbf{M}\boldsymbol{\Sigma}\boldsymbol{\Phi} = \mathbf{Q} \ ,$$
$$\boldsymbol{\Phi} = \mathbf{D}\boldsymbol{\Psi} \ , \quad (50)$$

where

- $\mathbf{L}$ = transport matrix from the streaming and the total collision terms
- $\boldsymbol{\Sigma}$ = scattering mass matrix that operates on the flux moments
- $\mathbf{M}$ = moment-to-direction matrix
- $\mathbf{D}$ = direction-to-moment matrix (typically, $\mathbf{D} = \mathbf{M}^T\mathbf{w}$, where $\mathbf{w}$ is the diagonal matrix containing the directional weights).

The external source is $\mathbf{Q}$. The dimensions of $\mathbf{L}$ are the number of spatial degrees of freedom times the number of directions, $(N_{dof} \times M)^2$; in a discontinuous method, the number of degrees of freedom is simply the number of elements N_{el} times the number of unknowns per element, i.e., $N_{dof} = N_{el} \times N(p)$, assuming a uniform polynomial order p is employed. For triangular meshes, $N(p) = (p+1)(p+2)/2$. The dimensions of $\boldsymbol{\Sigma}$ are $(N_{dof} \times N_{mom})^2$, where N_{mom} is the number of moments employed in the spherical harmonics expansion of the angular fluxes; letting N_a denote the anisotropic order, N_{mom} is equal to $(N_a+1)(N_a+2)/2$ in 2-D and equal to $(N_a+1)^2$ in 3-D for standard angular quadratures. In this paper, $N_a = 0$ and $N_{mom} = 1$. $\mathbf{D}$ is of dimension $(N_{dof} \times N_{mom}) \times (N_{dof} \times M)$; $\mathbf{M}$ is of dimension $(N_{dof} \times M) \times (N_{dof} \times N_{mom})$.

If reflecting or periodic boundaries are present (or more generally if the graph of the sweep presents dependencies), we practically break the transport sweep on these boundaries and introduce the notion of SAFs. In this situation, we define a matrix $\mathbf{N}$ that extracts from the entire angular flux vector all outgoing angular fluxes on the boundaries causing a dependency in the graph of the sweep; i.e., the SAF vector is given by

$$\boldsymbol{\Psi}_{\mathbf{SAF}} = \mathbf{N}\boldsymbol{\Psi} \ . \quad (51)$$

The dimension of $\boldsymbol{\Psi}_{\mathbf{SAF}}$ is N_{SAF}; the dimension of $\mathbf{N}$ is $N_{\mathrm{SAF}} \times (N_{dof} \times M)$. We then split the loss and streaming operator $\mathbf{L}$ into two parts:

$$\mathbf{L} = \underline{\mathbf{L}} - \bar{\mathbf{L}} \ , \quad (52)$$

where $\underline{\mathbf{L}}$ is the lower block triangular matrix (which can be inverted in one transport sweep) and $\bar{\mathbf{L}}$ is the strictly upper triangular block, causing the dependencies in the sweep. Note that we have

$$\bar{\mathbf{L}}\boldsymbol{\Psi} = \bar{\mathbf{L}}\mathbf{N}^T\mathbf{N}\boldsymbol{\Psi} = \bar{\mathbf{L}}\mathbf{N}^T\boldsymbol{\Psi}_{\mathbf{SAF}} \ , \quad (53)$$

and can, therefore, recast the transport equation as

$$\underline{\mathbf{L}}\boldsymbol{\Psi} = \bar{\mathbf{L}}\mathbf{N}^T\boldsymbol{\Psi}_{\mathbf{SAF}} + \mathbf{M}\boldsymbol{\Sigma}\boldsymbol{\Phi} + \mathbf{Q}$$

and

$$\boldsymbol{\Phi} = \mathbf{D}\boldsymbol{\Psi} \ . \quad (54)$$

Finally, during one SI iteration, the scalar flux and the angular significant flux are updated as follows:

$$\begin{bmatrix}\boldsymbol{\Phi}\\ \boldsymbol{\Psi}_{\mathbf{SAF}}\end{bmatrix}^{(\ell+1/2)} = \begin{bmatrix}\mathbf{D}\underline{\mathbf{L}}^{-1}\mathbf{M}\boldsymbol{\Sigma} & \mathbf{D}\underline{\mathbf{L}}^{-1}\bar{\mathbf{L}}\mathbf{N}^T\\ \mathbf{N}\underline{\mathbf{L}}^{-1}\mathbf{M}\boldsymbol{\Sigma} & \mathbf{N}\underline{\mathbf{L}}^{-1}\bar{\mathbf{L}}\mathbf{N}^T\end{bmatrix}\begin{bmatrix}\boldsymbol{\Phi}\\ \boldsymbol{\Psi}_{\mathbf{SAF}}\end{bmatrix}^{(\ell)} + \begin{bmatrix}\mathbf{D}\\ \mathbf{N}\end{bmatrix}\underline{\mathbf{L}}^{-1}\mathbf{Q} \ . \quad (55)$$

For completeness, we note that Eq. (55) represents precisely the matrix solution of the weak form given in Eq. (11). Equation (55) is simply coded by appending the $\boldsymbol{\Psi}_{\mathbf{SAF}}$ to the scalar flux unknowns (after a transport sweep, the operator $\mathbf{D}$ is applied to yield the newest scalar

flux whereas the operator $\mathbf{N}$ is applied to update the SAF). Note that when $\bar{\mathbf{L}} = 0$ (i.e., no dependencies in the sweep), we obtain the standard SI formula:

$$\mathbf{\Phi}^{(\ell+1/2)} = \mathbf{D}\underline{\mathbf{L}}^{-1}(\mathbf{M}\mathbf{\Sigma}\mathbf{\Phi}^{(\ell)} + \mathbf{Q}) \ . \tag{56}$$

From the SI formula of Eq. (55), it follows that the linear system for GMRes-based transport solves is simply

$$(\mathbf{I} - \mathbf{T})\mathbf{x} = \mathbf{b} \ , \tag{57}$$

where

$$\mathbf{T} = \begin{bmatrix} \mathbf{D}\underline{\mathbf{L}}^{-1}\mathbf{M}\mathbf{\Sigma} & \mathbf{D}\underline{\mathbf{L}}^{-1}\bar{\mathbf{L}}\mathbf{N}^T \\ \mathbf{N}\underline{\mathbf{L}}^{-1}\mathbf{M}\mathbf{\Sigma} & \mathbf{N}\underline{\mathbf{L}}^{-1}\bar{\mathbf{L}}\mathbf{N}^T \end{bmatrix} \ , \tag{58}$$

$$\mathbf{x} = \begin{bmatrix} \mathbf{\Phi} \\ \mathbf{\Psi}_{\mathbf{SAF}} \end{bmatrix} \ , \tag{59}$$

and

$$\mathbf{b} = \begin{bmatrix} \mathbf{D} \\ \mathbf{N} \end{bmatrix} \underline{\mathbf{L}}^{-1}\mathbf{Q} \ . \tag{60}$$

II.F.2. Diffusion Synthetic Acceleration–Accelerated Transport Solves

We now seek a matrix notation for the diffusion approximation of the synthetic acceleration forms, given previously as the DCF, IP, or MIP forms [Eqs. (35), (44), and (48), respectively]. The synthetic acceleration process can be cast generally as

$$\mathbf{x}^{(\ell+1/2)} = \mathbf{T}\mathbf{x}^{(\ell)} + \mathbf{b} \ , \tag{61}$$

$$\delta\mathbf{x} = \mathbf{P}\mathbf{A}^{-1}\mathbf{B}\mathbf{R}(\mathbf{x}^{(\ell+1/2)} - \mathbf{x}^{(\ell)}) \ , \tag{62}$$

and

$$\mathbf{x}^{(\ell+1)} = \mathbf{x}^{(\ell+1/2)} + \delta\mathbf{x} \ . \tag{63}$$

The operator $\mathbf{R}$ restricts the successive iterates in the scalar flux and SAF [i.e., $\mathbf{x}^{(\ell+1/2)} - \mathbf{x}^{(\ell)}$] to quantities used in the linear forms of the DSA equations [specifically the difference in scalar fluxes $\delta\Phi^{(\ell)}$ and the incoming values J^{inc} and $\vec{\Upsilon}^{inc}$; see Eqs. (38), (39), and (40)]. The load matrix $\mathbf{B}$ computes the appropriate matrices (volumetric and edge source terms) in order to build the linear forms l for the various diffusion approximations. The bilinear diffusion form is represented by the matrix $\mathbf{A}$. The dimension of $\mathbf{A}$ is $N_{dof} \times N_{dof}$. Note that these two matrices, $\mathbf{A}$ and $\mathbf{B}$, vary with each different diffusion scheme. Once the diffusion system has been solved for the corrective terms, these terms are prolongated onto the transport solution vector $\mathbf{x}$ using the operator $\mathbf{P}$ with Eqs. (18) and (19a). Therefore, any synthetic acceleration scheme employed with SI can be written as

$$\begin{aligned} \mathbf{x}^{(\ell+1)} &= \mathbf{x}^{(\ell+1/2)} + \delta\mathbf{x}^{(\ell)} \\ &= \mathbf{T}\mathbf{x}^{(\ell)} + \mathbf{b} + \mathbf{P}\mathbf{A}^{-1}\mathbf{B}\mathbf{R}(\mathbf{x}^{(\ell+1/2)} - \mathbf{x}^{(\ell)}) \\ &= \mathbf{x}^{(\ell)} - (\mathbf{I} + \mathbf{P}\mathbf{A}^{-1}\mathbf{B}\mathbf{R})(\mathbf{I} - \mathbf{T})\mathbf{x}^{(\ell)} \\ &\quad + (\mathbf{I} + \mathbf{P}\mathbf{A}^{-1}\mathbf{B}\mathbf{R})\mathbf{b} \ , \end{aligned} \tag{64}$$

which is precisely a preconditioned Richardson iteration with $\mathbf{I} + \mathbf{P}\mathbf{A}^{-1}\mathbf{B}\mathbf{R}$ as the preconditioner. The preconditioned GMRes solution technique employs

$$(\mathbf{I} + \mathbf{P}\mathbf{A}^{-1}\mathbf{B}\mathbf{R})(\mathbf{I} - \mathbf{T})\mathbf{x} = (\mathbf{I} + \mathbf{P}\mathbf{A}^{-1}\mathbf{B}\mathbf{R})\mathbf{b} \ , \tag{65}$$

where the iteration matrix with DSA is $\mathbf{I} - (\mathbf{I} + \mathbf{P}\mathbf{A}^{-1}\mathbf{B}\mathbf{R})(\mathbf{I} - \mathbf{T})$. Without DSA, it is simply $(\mathbf{I} - \mathbf{T})$.

In the above, the diffusion matrix $\mathbf{A}$ needs to be inverted. For the IP and MIP forms, this matrix is SPD and a CG technique, preconditioned with SSOR, is chosen. For the DCF form, we use the SQMR solver, preconditioned with SSOR as well. It is worthwhile to point out that the CG, the SQMR, and the SSOR solves are performed in a matrix-free form; i.e., the matrices are never explicitly formed but only the action of the matrix on a vector is required. This matrix-free implementation was found to be useful, especially in the case of AMR meshes.

III. FOURIER ANALYSIS

To analyze the performance of acceleration schemes, it is customary to carry out a Fourier analysis on the discretized equations. A large body of work exists in the transport community regarding the application of Fourier analysis to SI accelerated with DSA (Refs. 13, 14, and 15). Oftentimes, this is done for a periodic homogeneous domain. We present here our Fourier analysis of the various DFE diffusion schemes used to accelerate the DFE S_N transport equation. The error modes are decomposed into Fourier modes characterized by wave numbers $\vec{\Lambda} = [\lambda_x, \lambda_y]$. The damping of these error modes during one step of SI + DSA provides insight into the effectiveness of the acceleration method. The largest damping factor over all wave numbers corresponds to the spectral radius of the method. The smaller the spectral radius, the faster the iterations will converge. If the spectral radius is greater than 1, the scheme is unstable. Additional details regarding implementation of Fourier analysis to study DSA-accelerated SI schemes can be found in Ref. 14.

The Fourier analysis was carried out on a periodic rectangular domain of size $X \times Y$, divided into $n_x \times n_y$ smaller cells, where n_i is the number of uniform subdivisions along the i'th axis ($X = n_x \Delta x$, $Y = n_y \Delta y$). Each rectangular cell is cut into two triangular cells. Different triangular cells may contain different media. The Fourier analysis was performed using linear DFEs ($p = 1$) (but

higher-order finite elements have been implemented in our AMR transport code). In our Fourier analysis, the transport matrix $\mathbf{L}$ is inverted directly; hence, no SAFs are present. Wave numbers are chosen in the interval $[0, 2\pi/X) \otimes [0, 2\pi/Y)$. The spectral radius is defined as the largest eigenvalue of the iteration matrix over the entire range of wave numbers. This iteration matrix is given by $(\mathbf{I} - \mathbf{T})$, Eq. (57), for the unpreconditioned SI process and by $\mathbf{I} - (\mathbf{I} + \mathbf{PA}^{-1}\mathbf{BR})(\mathbf{I} - \mathbf{T})$, Eq. (64), for the DSA-SI process. The eigenvalues can easily be calculated in MATLAB using the built-in function `eig`, and the Nelder-Mead simplex algorithm is used to find the maximum eigenvalue over all possible wavelength numbers in $[0, 2\pi/X) \otimes [0, 2\pi/Y)$ for a given problem configuration.

III.A. Infinite Homogeneous Medium Case

In this example, we carry out a Fourier analysis for a 1×1 Cartesian geometry (i.e., two triangles). The same medium is placed in these two elements. The domain is square, i.e., $X = Y$, and the mesh size X is varied from 2^{-10} to 2^{10} mean free paths (mfp's). Periodic boundary conditions are applied on all four sides. Scattering is isotropic with a scattering ratio fixed to $c = 0.9999$. Level-symmetric (LS) angular quadrature sets S_2, S_4, S_8, and

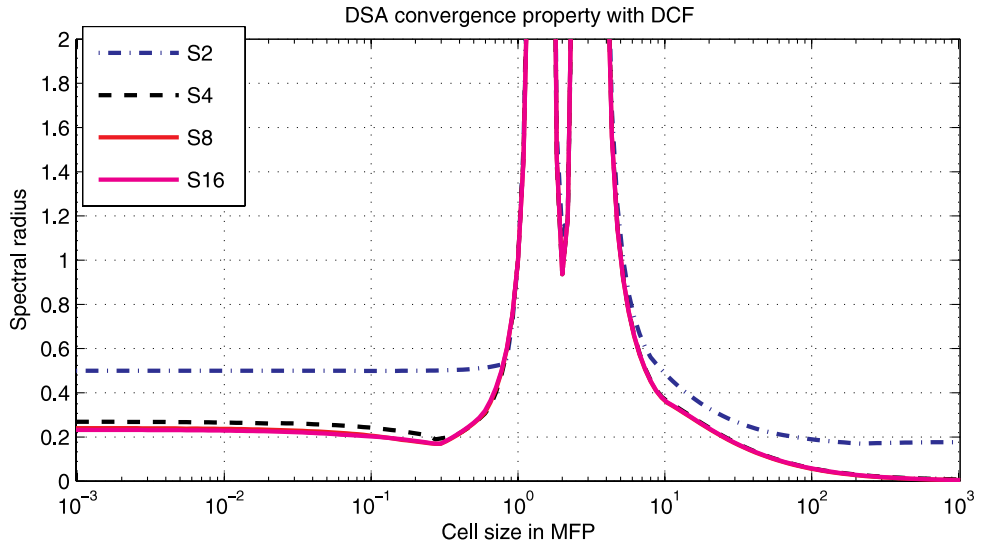

Fig. 1. Fourier analysis for the DCF form as a function of the mesh optical thickness, homogeneous infinite medium case.

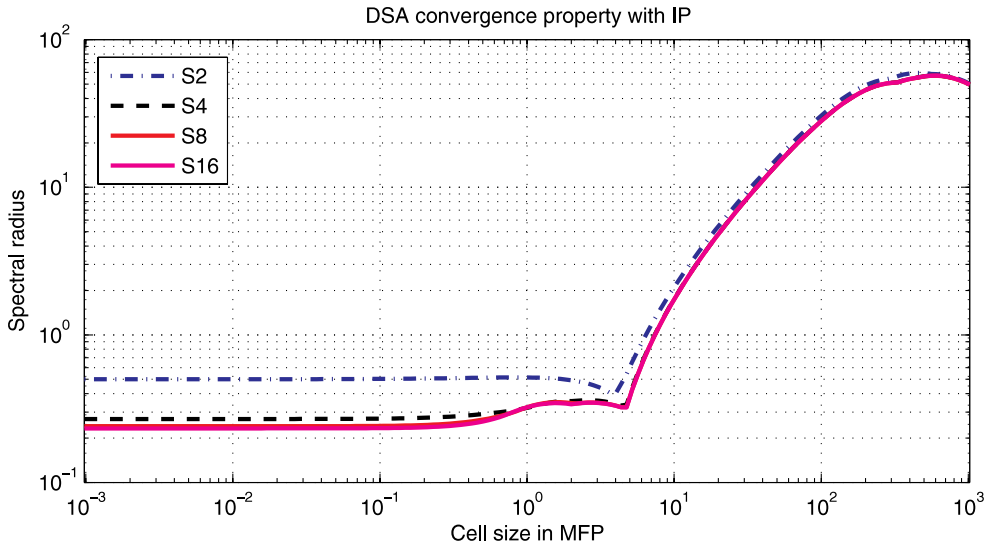

Fig. 2. Fourier analysis for the IP form as a function of the mesh optical thickness, homogeneous infinite medium case.

S_{16} are used. The following three DSA schemes are examined: DCF, IP, and MIP. Figures 1, 2, and 3 give the spectral radii obtained using these three schemes. There are four curves on each plot corresponding to the four different angular quadrature sets. The x-axis is the mesh size, measured in mfp; the y-axis is the spectral radius.

Both DCF and IP forms are not unconditionally stable: The DCF form is unstable in the intermediate mfp range, when cells are a few mfp's thick; the IP form is unstable for thick cells, when their cell sizes correspond to an edge penalty factor of about $\frac{1}{4}$. The MIP form is stable for all cell sizes, with the maximum spectral radius occurring in the intermediate mfp range: The maximum spectral radius is less than 0.47, except for S_2 where it is about 0.7. These results for MIP are very satisfactory and signify that the MIP-DSA form is capable of providing good acceleration, at least in the case of an infinite homogeneous problem. Results employing the IP form will no longer be presented, since the MIP form is clearly better. We also note that for thin cells, the spectral radius approaches the theoretical value of $0.2247c$ as the angular quadrature order is increased. Values of the spectral radius obtained with the four different S_N sets are 0.4999, 0.2689, 0.2401, and 0.2322, respectively; these values are in very good agreement with Fourier analysis for the analytic (i.e., not spatially discretized)

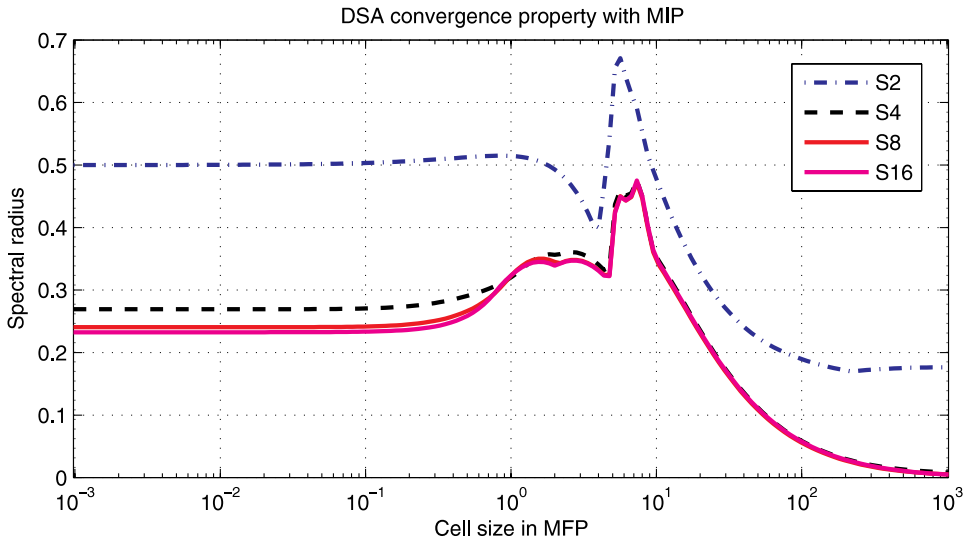

Fig. 3. Fourier analysis for the MIP form as a function of the mesh optical thickness, homogeneous infinite medium case.

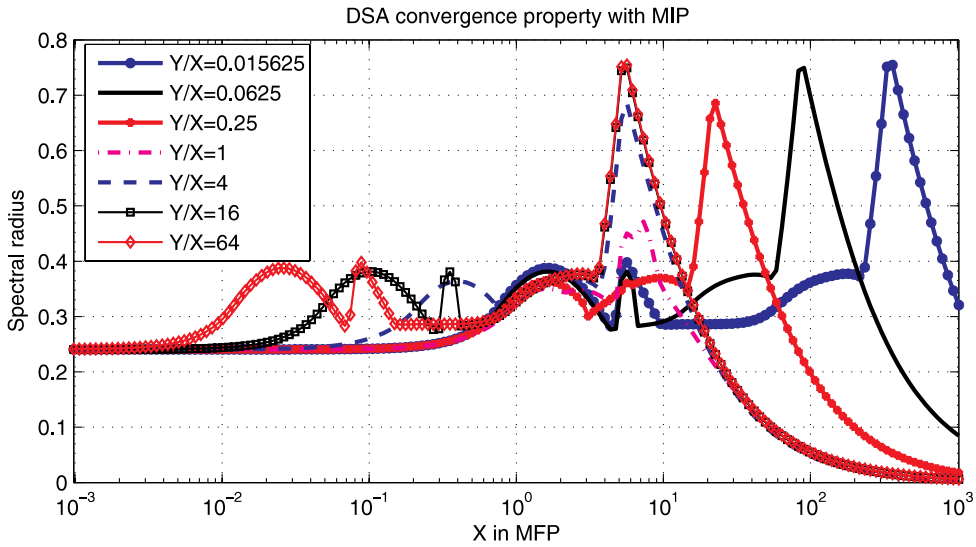

Fig. 4. Spectral radius for the MIP form with different aspect ratios.

S_N transport equation.[25] It is also worthwhile to recall that the M4S method is also not stable in the intermediate mfp range on unstructured meshes, as reported in Ref. 14; this is a behavior similar to that of the DCF form presented here.

Next, we analyze the MIP form for different cell aspect ratios by fixing $X = 1$ and changing the value of Y. Results using S_8 are shown in Fig. 4. They indicate that the MIP scheme converges, even for high aspect ratio cells.

III.B. Periodic Horizontal Interface Problem

The periodic horizontal interface (PHI) problem[26] is a standard litmus test for DSA techniques, notably to assess the effectiveness of the acceleration for highly heterogeneous configurations. The PHI problem consists of horizontal stripes of alternating transparent and highly diffusive media. In our test, two layers are employed. The first layer is optically thick, and the other layer is optically thin. This is achieved by setting $\sigma_{t,1} = \sigma$ and $\sigma_{t,2} = 1/\sigma$ and increasing the value of σ. Strong material discontinuities are present in this problem when σ becomes large, which could potentially reduce the effectiveness of the DSA schemes. Tests were run with various LS quadratures; without loss of generality, only the S_8 LS results are presented. Various values of scattering ratios are chosen: $c = \{0.9, 0.99, 0.999, 0.9999, 0.99999, 0.999999\}$. The study was conducted with a sequence of $\sigma = \{10, 20, 40, 80, 160, 320, 640\}$. Table I displays the spectral radius obtained with the MIP-DSA scheme for different scattering ratios. It can be seen that the MIP-DSA form loses effectiveness when the heterogeneity is strong, with the spectral radius tending toward c. This is similar to the loss of effectiveness observed in the presence of large material discontinuities.[27]

IV. NUMERICAL RESULTS

In this section, we report on the implementation of the three proposed DSA schemes in a 2-D mesh adaptive transport solver, XUTHUS. More details regarding XUTHUS and S_N transport solves using AMR meshes can be found in Refs. 5 and 28. Test problems for heterogeneous material configurations, with vacuum and reflecting boundaries, are solved using structured and unstructured triangular meshes.

IV.A. Homogeneous Problem

The first test is a simple homogeneous problem with vacuum boundaries, similar to the homogeneous problem employed in the Fourier analysis of Sec. III. The computational mesh is shown in Fig. 5. Equal widths in x and y are used. Scattering is isotropic with a scattering ratio c equal to 0.9999, and the volumetric source is

TABLE I

Spectral Radius for the PHI Problem, MIP Form with S_8 (Fourier Analysis Results)

	Scattering Ratios					
σ	0.9	0.99	0.999	0.9999	0.99999	0.999999
10	0.6868	0.8220	0.8541	0.8582	0.8586	0.8586
20	0.7716	0.9013	0.9278	0.9322	0.9327	0.9327
40	0.8167	0.9451	0.9629	0.9671	0.9676	0.9676
80	0.8434	0.9651	0.9811	0.9837	0.9841	0.9837
160	0.8580	0.9744	0.9900	0.9918	0.9922	0.9923
320	0.8656	0.9793	0.9942	0.9959	0.9962	0.9962
640	0.8696	0.9827	0.9962	0.9979	0.9981	0.9981

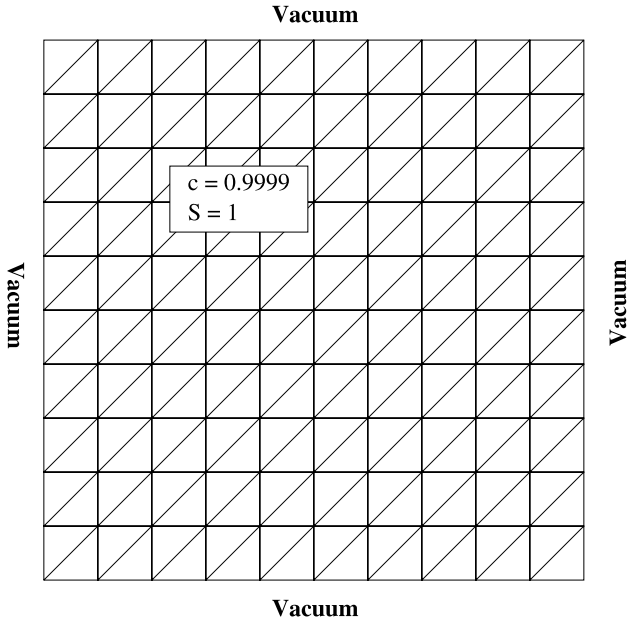

Fig. 5. Domain of the homogeneous DSA test problem computed with XUTHUS.

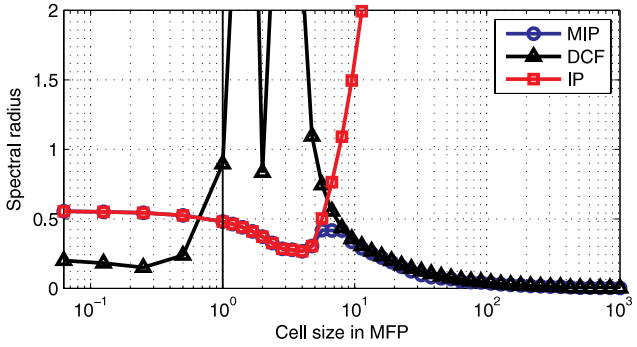

Fig. 6. NSR computed with XUTHUS for various DSA schemes.

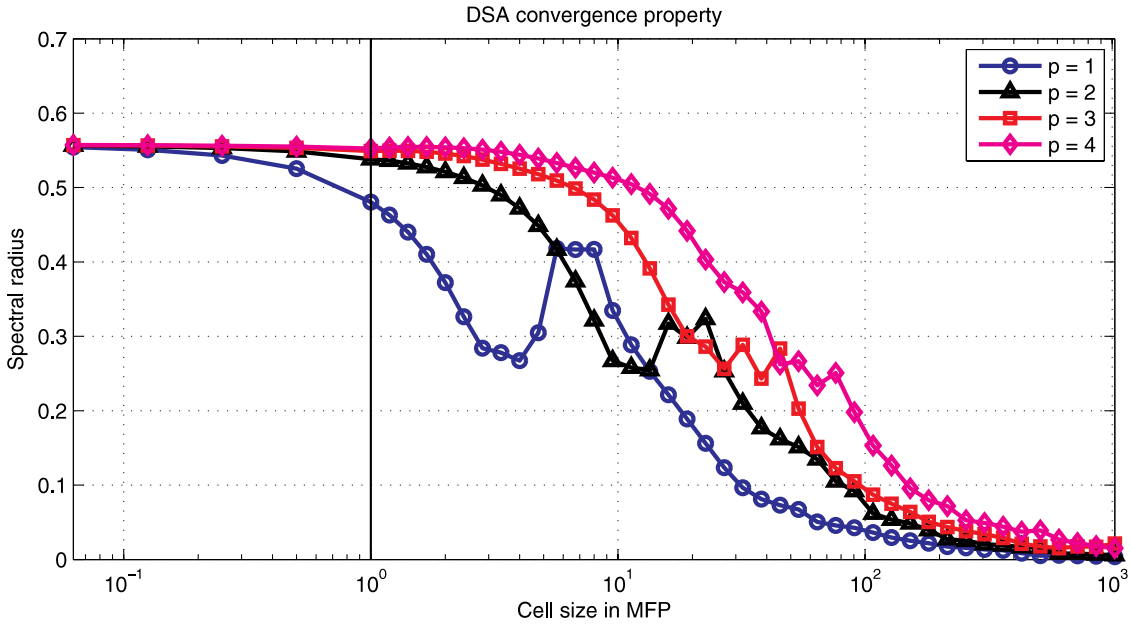

Fig. 7. NSR computed with XUTHUS for the MIP form using different polynomial orders.

uniform and isotropic. All computations employ an S_8 LS angular quadrature.

Calculations with different cell optical thicknesses are performed. For cases with cells thicker than 1 mfp, a fixed number of elements is used. In this situation, the square domain is cut into 200 triangular elements, and the domain size is fixed to 10 cm × 10 cm. The cells' optical thickness is changed by varying the total cross section σ_t from 1 cm^{-1} to 2^{10} cm^{-1}. For cases with cells thinner than 1 mfp, we keep the total cross section equal to 1 cm^{-1}, and the domain size is unchanged. By doing so, the domain size in mfp does not change; i.e., the leakage through the vacuum boundaries does not change. The cell size is reduced through uniform mesh refinement (where each element is subdivided into four smaller elements). Each refinement cycle decreases the cell size by a factor of 2, resulting in optically thinner cells.

The various numerical spectral radii (NSR) obtained for the different DSA schemes are provided in Fig. 6. Diffusion calculations are converged tightly, and enough SIs are performed to avoid errors in estimating the spectral radius. It can be clearly noted that XUTHUS produces results very similar to the Fourier analysis results. The DCF diverges for cell sizes in the intermediate

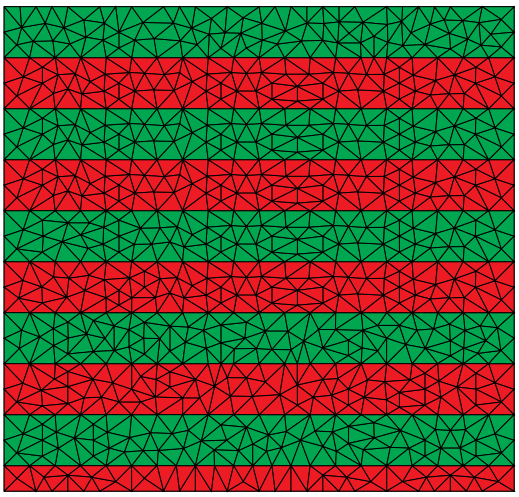

Fig. 8. Geometry and mesh for the PHI problem computed with XUTHUS.

TABLE II

Spectral Radius for the PHI Problem, MIP Form with S_8 (XUTHUS Runs)

	Scattering Ratios					
σ	0.9	0.99	0.999	0.9999	0.99999	0.999999
10	0.6607	0.7825	0.8221	0.8380	0.8417	0.8420
20	0.7534	0.8757	0.9043	0.9179	0.9176	0.9201
40	0.8098	0.9277	0.9501	0.9569	0.9599	0.9604
80	0.8423	0.9546	0.9736	0.9778	0.9797	0.9802
160	0.8619	0.9679	0.9850	0.9881	0.9885	0.9887
320	0.8749	0.9764	0.9902	0.9920	0.9914	0.9923
640	0.8827	0.9817	0.9926	0.9921	0.9942	0.9953

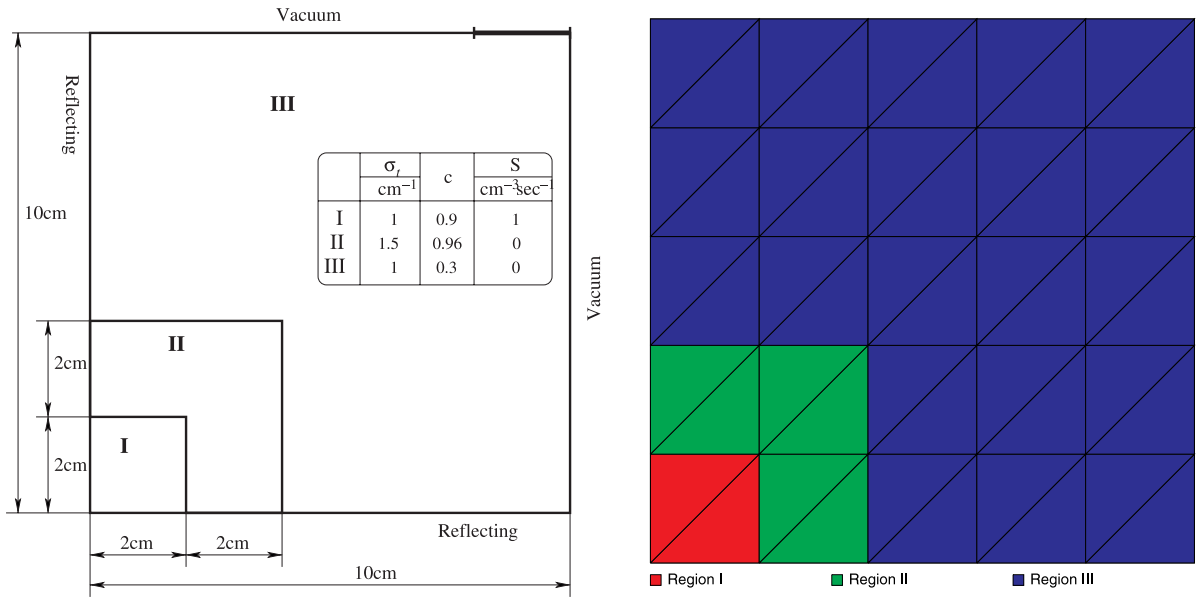

(a) (b)

Fig. 9. AMR test problem: (a) geometry and material description; (b) initial mesh.

TABLE III

Results with Bootstrapping and 1-Irregularity

Adaptivity Iteration Number	Number of Active Cells	Irregularity Index	NSR	Number of DSA Iterations	CPU Time in DSA (s)	Time Fraction of DSA	Relative Error in the Scalar Flux
0	50	0.0000	0.3157	75	0.01	0.500	1.167×10^{-2}
1	74	0.0412	0.2437	75	0.01	0.625	4.337×10^{-3}
2	104	0.0725	0.3408	65	0.02	0.529	2.624×10^{-3}
3	122	0.1118	0.3663	60	0.02	0.526	1.961×10^{-3}
4	206	0.1624	0.3205	90	0.05	0.667	9.156×10^{-4}
5	278	0.1220	0.3400	91	0.07	0.720	4.495×10^{-4}
6	356	0.1148	0.3105	112	0.11	0.711	3.593×10^{-4}
7	500	0.1759	0.3193	108	0.15	0.739	2.374×10^{-4}
8	824	0.1665	0.2701	92	0.21	0.732	1.284×10^{-4}
9	1 136	0.1582	0.3687	150	0.46	0.790	9.440×10^{-5}
10	1 586	0.1494	0.2276	73	0.32	0.703	5.768×10^{-5}
11	2 216	0.1619	0.2833	138	0.83	0.787	3.962×10^{-5}
12	3 188	0.1670	0.2038	61	0.56	0.695	2.521×10^{-5}
13	3 974	0.1663	0.2071	65	0.75	0.708	1.930×10^{-5}
14	5 318	0.1659	0.2118	59	1.00	0.684	1.430×10^{-5}
15	7 004	0.1708	0.1983	56	1.31	0.666	1.054×10^{-5}
16	8 918	0.1755	0.2014	45	1.41	0.613	7.725×10^{-6}
17	11 492	0.1831	0.1994	34	1.46	0.551	6.228×10^{-6}
18	14 492	0.1793	0.1343	19	1.09	0.469	4.788×10^{-6}
19	18 296	0.1799	0.1359	23	1.65	0.512	3.650×10^{-6}
20	23 522	0.1861	0.1408	22	2.01	0.503	2.986×10^{-6}
21	28 214	0.1813	0.1393	23	2.52	0.513	2.407×10^{-6}
22	37 394	0.1823	0.1350	25	3.63	0.533	1.811×10^{-6}
23	46 940	0.1858	0.1352	22	4.13	0.507	1.424×10^{-6}
24	54 146	0.1858	0.0977	17	3.64	0.507	1.222×10^{-6}

mfp range while the IP form is unstable for thick cells. The NSR of the MIP form switches from the one obtained with the IP form (thin cell limit) to the one of the DCF form (thick cell limit), showing that MIP is stable over the entire range, from optically thin to optically thick cells. In comparison to the Fourier results, the presence of the Dirichlet boundary condition affects the NSR of the MIP scheme, but a good effectiveness is retained nonetheless.

The effect of polynomial order on the MIP form is analyzed (recall that the penalty coefficient in the MIP quadratically depends on the polynomial order p). For polynomial orders 1 through 4, the NSR results for DSA-MIP are plotted in Fig. 7, using an S_8 LS quadrature. We note that the DSA-MIP form is stable for all polynomial orders.

IV.B. Periodic Horizontal Interface Test

The second test is the PHI problem, similar to the PHI problem employed in the Fourier analysis of Sec. III.B. The computational mesh is shown in Fig. 8. The unstructured triangular mesh is generated with Triangle.[29] The left and bottom boundaries are reflecting; the right and top boundaries are vacuum. Two repeated layers are arranged as in Fig. 8. The red layers are optically thick, and the green layers are optically thin (color online). The study was conducted with a sequence of total cross sections and various values of scattering ratios, as in the Fourier analysis case. An S_8 LS angular quadrature is used.

The NSRs are given in Table II. Again, it is noted that XUTHUS produces results very similar to the Fourier analysis results, with a degradation of the effectiveness of DSA for highly heterogeneous configurations.

IV.C. With Adaptive Mesh Refinement Hanging Nodes

Diffusion schemes based on DFEs can be used in a natural fashion with AMR techniques. The performance of the MIP-DSA form on irregular meshes stemming from AMR is analyzed next. The geometry, material data, and initial coarse mesh are given in Fig. 9. The polynomial order used is 2 for all elements, an S_4 LS angular quadrature is employed, and the scattering and the external source are isotropic. The AMR calculation is carried out, employing the technique described in Refs. 5 and 30. In essence, the mesh refinement process

TABLE IV

Results with Bootstrapping and 2-Irregularity

Adaptivity Iteration Number	Number of Active Cells	Irregularity Index	NSR	Number of DSA Iterations	CPU Time in DSA (s)	Time Fraction of DSA	Relative Error in the Scalar Flux
0	50	0.0000	0.3157	75	0.01	0.500	1.167×10^{-2}
1	74	0.0412	0.2437	75	0.01	0.583	4.337×10^{-3}
2	104	0.0725	0.3408	65	0.02	0.500	2.624×10^{-3}
3	122	0.1118	0.3663	60	0.02	0.513	1.961×10^{-3}
4	206	0.1624	0.3205	90	0.05	0.684	9.156×10^{-4}
5	278	0.1220	0.3400	91	0.07	0.676	4.495×10^{-4}
6	356	0.1148	0.3105	112	0.11	0.745	3.593×10^{-4}
7	500	0.1759	0.3193	108	0.15	0.740	2.374×10^{-4}
8	794	0.1693	0.2917	93	0.20	0.739	1.342×10^{-4}
9	1 112	0.1705	0.2790	117	0.35	0.772	8.982×10^{-5}
10	1 526	0.1506	0.2268	71	0.30	0.710	5.693×10^{-5}
11	2 174	0.1653	0.2786	142	0.84	0.804	3.916×10^{-5}
12	2 942	0.1660	0.2022	65	0.53	0.719	2.592×10^{-5}
13	3 716	0.1730	0.2051	67	0.71	0.728	1.965×10^{-5}
14	5 144	0.1875	0.2063	67	1.07	0.713	1.430×10^{-5}
15	6 848	0.1818	0.1978	38	0.85	0.588	9.766×10^{-6}
16	8 096	0.1850	0.2022	28	0.78	0.516	7.737×10^{-6}
17	10 328	0.1953	0.2038	38	1.35	0.579	6.113×10^{-6}
18	12 746	0.1955	0.1401	19	0.89	0.471	4.651×10^{-6}
19	15 476	0.1979	0.1365	25	1.39	0.530	3.654×10^{-6}
20	20 834	0.2104	0.1402	27	2.03	0.549	2.758×10^{-6}
21	26 060	0.2175	0.1477	22	2.26	0.505	2.147×10^{-6}
22	31 748	0.2123	0.1414	25	3.08	0.533	1.697×10^{-6}
23	41 138	0.2103	0.1461	26	4.18	0.543	1.284×10^{-6}
24	45 116	0.2082	0.1032	19	3.37	0.533	1.173×10^{-6}

is wrapped around the standard SI or GMRes iterations. At each adaptivity iteration, the DSA-preconditioned transport problem is solved. An error estimator evaluates the cellwise errors, and the cells with the largest errors are selected for refinement. Different levels of mesh irregularity are tested: 1-irregularity, 2-irregularity, and 3-irregularity. Here, *n*-irregularity signifies that the maximum refinement-level difference between two neighboring elements is at most *n*. For each level of mesh irregularity, two AMR runs are presented. One run is performed using solution-bootstrapping at each mesh adaptivity cycle; i.e., the numerical solution (scalar flux and SAFs) of the previous adapted mesh is projected onto the newly prescribed adapted mesh and serves as an initial guess. The other run is performed without bootstrapping, i.e., the initial guess is reset to zero at each mesh adaptivity iteration. Obviously, one would always prefer to use the previously obtained solution as an initial guess to bootstrap the iterative process on the newly refined mesh, but it is instructive to compare the performance of DSA on AMR meshes in both situations.

Six tables for the three different levels of mesh irregularity and the two different initialization strategies are displayed in Tables III through VIII. A total of 25 mesh adaptivity cycles are performed in each case. The second column in these tables shows the number of active elements at each adaptivity cycle. The third column is a mesh parameter measuring the mesh irregularity defined as the average number of hanging nodes on all active edges.

When reinitializing the solution at each adaptivity iteration (Tables VI through VIII), we note that the number of DSA iterations approximately increases by a factor of 2 each time the number of unknowns is increased by a factor of 4, which is to be expected for linear solves performed with the CG technique. As a consequence, the fraction of time spent in the DSA solver increases significantly as the AMR proceeds. On the other hand, when bootstrapping is employed at each adaptivity cycle, the number of DSA iterations remains very small, and as a result, the total computing time with AMR is significantly reduced. We conclude that not only the MIP-DSA preconditioner performs efficiently with AMR grids, but it also shows that there is a clear advantage in converging the preconditioned transport solves on coarse meshes first (which is computationally inexpensive) and employing the coarser solutions as a guess for the finer meshes. Our results show that the fraction of time spent in DSA

TABLE V

Results with Bootstrapping and 3-Irregularity

Adaptivity Iteration Number	Number of Active Cells	Irregularity Index	NSR	Number of DSA Iterations	CPU Time in DSA (s)	Time Fraction of DSA	Relative Error in the Scalar Flux
0	50	0.0000	0.3157	75	0.01	0.500	1.167×10^{-2}
1	74	0.0412	0.2437	75	0.01	0.609	4.337×10^{-3}
2	104	0.0725	0.3408	65	0.02	0.529	2.624×10^{-3}
3	122	0.1118	0.3663	60	0.02	0.564	1.961×10^{-3}
4	206	0.1624	0.3205	90	0.05	0.671	9.156×10^{-4}
5	278	0.1220	0.3400	91	0.07	0.699	4.495×10^{-4}
6	356	0.1148	0.3105	112	0.11	0.720	3.593×10^{-4}
7	500	0.1759	0.3193	108	0.15	0.744	2.374×10^{-4}
8	794	0.1693	0.2917	93	0.21	0.736	1.342×10^{-4}
9	1 112	0.1705	0.2790	117	0.36	0.778	8.982×10^{-5}
10	1 526	0.1506	0.2268	71	0.31	0.710	5.693×10^{-5}
11	2 162	0.1663	0.2755	141	0.84	0.793	3.918×10^{-5}
12	2 942	0.1660	0.2021	65	0.55	0.714	2.595×10^{-5}
13	3 710	0.1737	0.2055	67	0.73	0.718	1.968×10^{-5}
14	5 108	0.1871	0.2069	68	1.10	0.715	1.432×10^{-5}
15	6 764	0.1838	0.2011	54	1.25	0.663	9.852×10^{-6}
16	8 006	0.1883	0.2026	34	0.97	0.557	7.778×10^{-6}
17	10 256	0.1968	0.2041	38	1.42	0.582	6.117×10^{-6}
18	12 656	0.1992	0.1401	20	0.98	0.483	4.663×10^{-6}
19	15 332	0.2003	0.1364	25	1.49	0.533	3.644×10^{-6}
20	20 384	0.2116	0.1410	28	2.19	0.561	2.743×10^{-6}
21	24 626	0.2161	0.1458	23	2.24	0.517	2.205×10^{-6}
22	27 266	0.2167	0.1458	25	2.72	0.536	1.948×10^{-6}
23	33 038	0.2157	0.1497	25	3.29	0.536	1.526×10^{-6}
24	42 770	0.2180	0.1027	21	3.53	0.558	1.138×10^{-6}

TABLE VI

Results with Reinitialization and 1-Irregularity

Adaptivity Iteration Number	Number of Active Cells	Irregularity Index	NSR	Number of DSA Iterations	CPU Time in DSA (s)	Time Fraction of DSA	Relative Error in the Scalar Flux
0	50	0.0000	0.3157	75	0.01	0.478	1.167×10^{-2}
1	74	0.0412	0.3181	128	0.03	0.634	4.337×10^{-3}
2	104	0.0725	0.3108	133	0.04	0.656	2.624×10^{-3}
3	122	0.1118	0.3372	151	0.05	0.662	1.961×10^{-3}
4	206	0.1624	0.3046	238	0.13	0.749	9.156×10^{-4}
5	278	0.1220	0.3204	282	0.21	0.787	4.495×10^{-4}
6	356	0.1148	0.3411	318	0.29	0.806	3.593×10^{-4}
7	500	0.1759	0.3422	367	0.48	0.810	2.374×10^{-4}
8	824	0.1665	0.3504	469	1.02	0.849	1.284×10^{-4}
9	1 136	0.1582	0.3464	545	1.62	0.868	9.440×10^{-5}
10	1 586	0.1494	0.3441	657	2.76	0.874	5.768×10^{-5}
11	2 216	0.1619	0.3593	814	4.74	0.895	3.962×10^{-5}
12	3 188	0.1670	0.3957	957	8.10	0.912	2.521×10^{-5}
13	3 974	0.1663	0.3576	1032	10.81	0.919	1.930×10^{-5}
14	5 318	0.1659	0.3731	1194	17.52	0.923	1.430×10^{-5}
15	7 004	0.1708	0.3761	1310	26.96	0.925	1.054×10^{-5}
16	8 918	0.1755	0.3687	1561	42.92	0.932	7.725×10^{-6}
17	11 486	0.1831	0.3844	1849	71.43	0.938	6.230×10^{-6}
18	14 492	0.1793	0.3857	2162	107.53	0.947	4.788×10^{-6}
19	18 296	0.1799	0.3795	2371	147.29	0.952	3.650×10^{-6}
20	23 516	0.1860	0.3571	2617	204.23	0.957	2.986×10^{-6}
21	28 226	0.1814	0.3788	3084	290.09	0.963	2.408×10^{-6}
22	37 382	0.1824	0.3646	3266	412.18	0.965	1.813×10^{-6}
23	46 994	0.1858	0.3750	3375	537.60	0.966	1.425×10^{-6}
24	54 194	0.1858	0.4286	3819	703.51	0.969	1.223×10^{-6}

remains small and constant throughout the AMR cycles. We provide several selected adapted meshes from the 2-irregularity runs in Fig. 10.

V. CONCLUSIONS

We have derived DSA schemes for the S_N transport equations discretized with high-order DFEs (even though we presented the derivation for isotropic scattering only, the extension to include anisotropic scattering is straightforward to derive). The DSA schemes have been obtained directly from the discretized transport equations and, therefore, provide straightforwardly discontinuous corrective terms to accelerate the transport iterations. These schemes belong to the partially consistent family of DSA techniques, as we have only used the zeroth angular moment of the transport equation and have

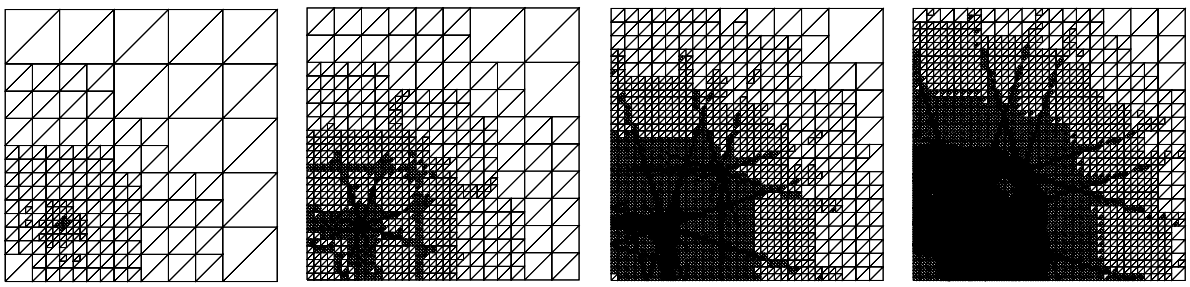

(a) Cycle #6 (b) Cycle #12 (c) Cycle #18 (d) Cycle #24

Fig. 10. AMR meshes obtained for the problem described in Fig. 9.

TABLE VII

Results with Reinitialization and 2-Irregularity

Adaptivity Iteration Number	Number of Active Cells	Irregularity Index	NSR	Number of DSA Iterations	CPU Time in DSA (s)	Time Fraction of DSA	Relative Error in the Scalar Flux
0	50	0.0000	0.3157	75	0.01	0.435	1.167×10^{-2}
1	74	0.0412	0.3181	128	0.03	0.619	4.337×10^{-3}
2	104	0.0725	0.3108	133	0.04	0.655	2.624×10^{-3}
3	122	0.1118	0.3372	151	0.05	0.636	1.961×10^{-3}
4	206	0.1624	0.3046	238	0.14	0.763	9.156×10^{-4}
5	278	0.1220	0.3204	282	0.21	0.791	4.495×10^{-4}
6	356	0.1148	0.3411	318	0.30	0.809	3.593×10^{-4}
7	500	0.1759	0.3422	367	0.51	0.817	2.374×10^{-4}
8	794	0.1693	0.3403	464	1.00	0.852	1.342×10^{-4}
9	1 112	0.1705	0.3430	546	1.64	0.874	8.982×10^{-5}
10	1 526	0.1506	0.3964	637	2.61	0.888	5.693×10^{-5}
11	2 174	0.1653	0.3471	782	4.61	0.892	3.916×10^{-5}
12	2 942	0.1660	0.3465	890	7.12	0.906	2.592×10^{-5}
13	3 716	0.1730	0.3713	1005	10.30	0.909	1.965×10^{-5}
14	5 144	0.1875	0.3454	1124	17.62	0.918	1.430×10^{-5}
15	6 848	0.1818	0.3583	1286	27.96	0.926	9.766×10^{-6}
16	8 096	0.1850	0.3715	1546	40.71	0.934	7.738×10^{-6}
17	10 328	0.1953	0.3232	1617	56.29	0.939	6.113×10^{-6}
18	12 746	0.1955	0.3830	2021	88.13	0.946	4.651×10^{-6}
19	15 470	0.1976	0.3281	2035	108.61	0.951	3.655×10^{-6}
20	20 822	0.2100	0.3595	2401	175.32	0.958	2.758×10^{-6}
21	26 060	0.2170	0.3610	2499	230.80	0.960	2.147×10^{-6}
22	31 712	0.2120	0.3869	2862	322.72	0.961	1.700×10^{-6}
23	41 210	0.2108	0.3707	3437	493.13	0.968	1.283×10^{-6}
24	45 140	0.2081	0.3746	3318	526.14	0.967	1.172×10^{-6}

explicitly made use of Fick's law to eliminate the current unknowns. The diffusion coefficient and the absorption cross section used in the diffusion equation are obtained naturally in the derivation. Because of the discontinuous nature of the spatial approximation for the DSA equations, locally refined meshes can easily be handled, and these DSA schemes are suitable for transport solves performed on AMR grids. We also note that the discontinuous diffusion equations hereby derived can be related to the IP method. A Fourier analysis has been carried out to determine the convergence properties of the proposed DSA schemes for various cell optical thicknesses and aspect ratios.

Out of the three DSA schemes derived, the MIP scheme (MIP-DSA) is stable and effective for realistic problems, even with distorted elements but loses effectiveness for highly heterogeneous configurations, similarly to other partially consistent DSA schemes (e.g., the WLA scheme). The MIP-DSA scheme is SPD, and a standard CG technique (preconditioned with SSOR) is used to solve the linear system. The MIP-DSA has been implemented in a 2-D AMR S_N transport code, and the numerical results obtained are in good agreement with the Fourier analysis. The implementation of DSA has been performed for both SI and GMRes-based iterations, with polynomial orders up to 4. Results on AMR grids show that the cost of DSA can be kept low as meshes become locally refined during the AMR process.

APPENDIX

WEIGHTED-RESIDUAL FORMULA FOR ONE DIRECTION

The weak variational form of the transport equation given in Eq. (5) was based on the one-direction weak form, which we provide in this Appendix. Consider a DFE discretization of the transport equation for one angular direction $\vec{\Omega}_m$ and one spatial element K of mesh $\mathbb{T}_h$. We multiply the transport equation Eq. (1) with a test function $\Psi_m^* \in V_p(K)$ and integrate over element K. The streaming term $(\vec{\Omega}_m \cdot \vec{\nabla})$ is integrated by parts, and a standard upwinding procedure is employed for the flux values on ∂K, the boundary of K. We thereby obtain

TABLE VIII

Results with Reinitialization and 3-Irregularity

Adaptivity Iteration Number	Number of Active Cells	Irregularity Index	NSR	Number of DSA Iterations	CPU Time in DSA (s)	Time Fraction of DSA	Relative Error in the Scalar Flux
0	50	0.0000	0.3157	75	0.01	0.435	1.167×10^{-2}
1	74	0.0412	0.3181	128	0.03	0.619	4.337×10^{-3}
2	104	0.0725	0.3108	133	0.04	0.638	2.624×10^{-3}
3	122	0.1118	0.3372	151	0.05	0.697	1.961×10^{-3}
4	206	0.1624	0.3046	238	0.13	0.753	9.156×10^{-4}
5	278	0.1220	0.3204	282	0.21	0.787	4.495×10^{-4}
6	356	0.1148	0.3411	318	0.30	0.806	3.593×10^{-4}
7	500	0.1759	0.3422	367	0.50	0.812	2.374×10^{-4}
8	794	0.1693	0.3403	464	1.00	0.851	1.342×10^{-4}
9	1 112	0.1705	0.3430	546	1.64	0.876	8.982×10^{-5}
10	1 526	0.1506	0.3964	637	2.59	0.889	5.693×10^{-5}
11	2 162	0.1663	0.3759	769	4.49	0.893	3.918×10^{-5}
12	2 942	0.1660	0.3464	890	7.06	0.909	2.595×10^{-5}
13	3 710	0.1737	0.3727	1005	10.56	0.913	1.968×10^{-5}
14	5 108	0.1871	0.2838	1090	16.43	0.926	1.432×10^{-5}
15	6 764	0.1838	0.3713	1248	25.91	0.924	9.852×10^{-6}
16	8 006	0.1883	0.3740	1529	38.67	0.933	7.779×10^{-6}
17	10 256	0.1968	0.3178	1663	56.12	0.941	6.117×10^{-6}
18	12 656	0.1992	0.3810	2000	85.25	0.945	4.664×10^{-6}
19	15 332	0.2003	0.3338	2021	105.80	0.951	3.645×10^{-6}
20	20 384	0.2116	0.3680	2354	167.26	0.958	2.743×10^{-6}
21	24 632	0.2160	0.3728	2614	225.27	0.958	2.203×10^{-6}
22	27 104	0.2180	0.3773	2745	262.45	0.960	1.962×10^{-6}
23	34 004	0.2165	0.4090	3110	364.24	0.964	1.479×10^{-6}
24	42 044	0.2138	0.3683	3135	455.50	0.964	1.155×10^{-6}

the Galerkin weighted-residual formula for a given angular direction $\vec{\Omega}_m$:

Find $\Psi_m \in V_p(K)$, such that $\forall \Psi_m^* \in V_p(K)$,

$$
\begin{aligned}
&(\Psi_m, (-\vec{\Omega}_m \cdot \vec{\nabla} + \sigma_t)\Psi_m^*)_K + \langle \Psi_m^-, \Psi_m^{*-} \rangle_{\partial K^+} \\
&\quad - \langle \Psi_m^-, \Psi_m^{*+} \rangle_{\partial K^- \setminus \partial \mathcal{D}} \\
&\quad - \langle \Psi_m^{inc}, \Psi_m^{*+} \rangle_{\partial K^- \cap \partial \mathcal{D}^d} - \langle \Psi_{m'}^+, \Psi_m^{*+} \rangle_{\partial K^- \cap \partial \mathcal{D}^r} \\
&= \frac{1}{4\pi} (\sigma_s \Phi, \Psi_m^*)_K + \frac{1}{4\pi} (Q, \Psi_m^*)_K \ , \qquad \text{(A.1)}
\end{aligned}
$$

where

∂K^- = inflow boundary

∂K^+ = outflow boundary.

The traces f^+ and f^- are defined with respect to the particle direction $\vec{\Omega}_m$, i.e., on an inflow boundary, f^+ (respectively f^-) is the value of f taken from within element K (respectively from the upwind neighbor), and on an outflow boundary, f^+ (respectively f^-) is the value of f taken from the downwind neighbor (respectively from within element K). The notations can be found in Eqs. (9) and (10). Upon a second integration by parts of the streaming term, we obtain the following:

Find $\Psi_m \in V_p(K)$, such that $\forall \Psi_m^* \in V_p(K)$,

$$
\begin{aligned}
&((\vec{\Omega}_m \cdot \vec{\nabla} + \sigma_t)\Psi_m, \Psi_m^*)_K + \langle [\![\Psi_m]\!], \Psi_m^{*+} \rangle_{\partial K^- \setminus \partial \mathcal{D}} \\
&\quad + \langle \Psi_m^+, \Psi_m^{*+} \rangle_{\partial K^- \cap \partial \mathcal{D}^d} - \langle \Psi_m^{inc}, \Psi_m^{*+} \rangle_{\partial K^- \cap \partial \mathcal{D}^d} \\
&\quad + \langle \Psi_m^+, \Psi_m^{*+} \rangle_{\partial K^- \cap \partial \mathcal{D}^r} - \langle \Psi_{m'}^+, \Psi_m^{*+} \rangle_{\partial K^- \cap \partial \mathcal{D}^r} \\
&= \frac{1}{4\pi} (\sigma_s \Phi, \Psi_m^*)_K + \frac{1}{4\pi} (Q, \Psi_m^*)_K \ , \qquad \text{(A.2)}
\end{aligned}
$$

where we recall the inter-element jump definition,

$$
[\![\Psi_m]\!] = \Psi_m^+ - \Psi_m^- \ . \qquad \text{(A.3)}
$$

By summing over all elements, we obtain

$$((\vec{\Omega}_m \cdot \vec{\nabla} + \sigma_t)\Psi_m, \Psi_m^*)_{\mathcal{D}} + \langle [\![\Psi_m]\!], \Psi_m^{*+} \rangle_{E_h^i} + \langle \Psi_m, \Psi_m^* \rangle_{\partial \mathcal{D}_m^-} - \langle \Psi_{m'}, \Psi_m^* \rangle_{\partial \mathcal{D}_m^{r-}} = \frac{1}{4\pi} (\sigma_s \Phi, \Psi_m^*)_{\mathcal{D}} + \langle \Psi_m^{inc}, \Psi_m^* \rangle_{\partial \mathcal{D}_m^{d-}} + \frac{1}{4\pi} (Q, \Psi_m^*)_{\mathcal{D}} \ . \quad \text{(A.4)}$$

Finally, using Eq. (A.4) and carrying out the weighted summation over all directions, we obtain Eq. (5).

REFERENCES

1. J. P. JESSEE, W. A. FIVELAND, L. H. HOWELL, P. COLELLA, and R. B. PEMBER, "An Adaptive Mesh Refinement Algorithm for the Radiative Transport Equation," *J. Comput. Phys.*, **139**, *2*, 380 (1998).

2. R. S. BAKER, "A Block Adaptive Mesh Refinement Algorithm for the Neutral Particle Transport Equation," *Nucl. Sci. Eng.*, **141**, 1 (2002).

3. C. AUSSOURD, "Styx: A Multidimensional AMR S_N Scheme," *Nucl. Sci. Eng.*, **143**, 281 (2003).

4. J. DUO, Y. AZMY, and L. ZIKATANOV, "A Posteriori Error Estimator and AMR for Discrete Ordinates Nodal Transport Methods," *Proc. Int. Conf. Physics of Reactors: Nuclear Power: A Sustainable Resource (PHYSOR 2008)*, Interlaken, Switzerland, September 14–19, 2008, American Nuclear Society (2008).

5. Y. WANG and J. RAGUSA, "Standard and Goal-Oriented Adaptive Mesh Refinement Applied to Radiation Transport on 2D Unstructured Triangular Meshes," *J. Comput. Phys.* (submitted for publication).

6. R. C. WARD, R. S. BAKER, and J. E. MOREL, "A Diffusion Synthetic Acceleration Method for Block Adaptive Mesh Refinement," *Nucl. Sci. Eng.*, **152**, 164 (2006).

7. T. A. WAREING, J. M. McGHEE, J. E. MOREL, and S. D. PAUTZ, "Discontinuous Finite Element S_N Methods on Three-Dimensional Unstructured Grids," *Nucl. Sci. Eng.*, **138**, 256 (2001).

8. Y. WANG and J. RAGUSA, "On the Convergence of DG-FEM Applied to the Discrete Ordinates Transport Equation for Structured and Unstructured Triangular Meshes," *Nucl. Sci. Eng.*, **163**, 56 (2009).

9. Y. WANG and J. RAGUSA, "A High-Order Discontinuous Galerkin Method for the S_N Transport Equations on 2D Unstructured Triangular Meshes," *Ann. Nucl. Energy*, **36**, 931 (2009).

10. R. E. ALCOUFFE, "Diffusion Synthetic Acceleration Methods for the Diamond-Differenced Discrete-Ordinates Equations," *Nucl. Sci. Eng.*, **64**, 344 (1977).

11. E. W. LARSEN, "Unconditionally Stable Diffusion-Synthetic Acceleration Methods for the Slab Geometry Discrete Ordinates Equations. Part I: Theory," *Nucl. Sci. Eng.*, **82**, 47 (1982).

12. D. R. McCOY and E. W. LARSEN, "Unconditionally Stable Diffusion-Synthetic Acceleration Methods for Slab Geometry Discrete Ordinates Equations. Part II: Numerical Results," *Nucl. Sci. Eng.*, **82**, 64 (1982).

13. E. W. LARSEN, "Diffusion-Synthetic Acceleration Methods for Discrete-Ordinates Problems," *Transp. Theory Stat. Phys.*, **13**, 107 (1984).

14. J. S. WARSA, T. A. WAREING, and J. E. MOREL, "Fully Consistent Diffusion Synthetic Acceleration of Linear Discontinuous S_N Transport Discretizations on Unstructured Tetrahedral Meshes," *Nucl. Sci. Eng.*, **141**, 236 (2002).

15. M. L. ADAMS and W. R. MARTIN, "Diffusion Synthetic Acceleration of Discontinuous Finite Element Transport Iterations," *Nucl. Sci. Eng.*, **111**, 145 (1992).

16. M. L. ADAMS and E. W. LARSEN, "Fast Iterative Methods for Discrete-Ordinates Particle Transport Calculations," *Prog. Nucl. Energy*, **40**, *1*, 3 (2002).

17. J. DOUGLAS and T. DUPONT, "Interior Penalty Procedures for Elliptic and Parabolic Galerkin Method," *Lecture Notes in Physics*, Vol. 58, Springer-Verlag (1976).

18. B. STAMM, "Spectral Discontinuous Galerkin Method for Hyperbolic Problems," Master's Thesis, Ecole Polytechnique Federale de Lausanne (2005).

19. W. STACEY, *Nuclear Reactor Physics*, Wiley Interscience (2001).

20. R. W. FREUND and N. M. NACHTIGAL, "QMRPACK: A Package of QMR Algorithms," *ACM Trans. Math. Softw.*, **22**, *1*, 46 (1996).

21. J. NITSCHE, "Über ein Variationsprinzip zur Lösung von Dirichlet-Problemen bei der Verwendung von Teilräumen, die keinen Randbedingungen unterworfen sind," *Abh. Math. Univ. Hamburg*, **36**, 9 (1971).

22. D. N. ARNOLD, "An Interior Penalty Finite Element Method with Discontinuous Elements," *SIAM J. Numer. Anal.*, **19**, 742 (1982).

23. G. KANSCHAT, *Discontinuous Galerkin Methods for Viscous Incompressible Flow*, Deutscher Universitäts-Verlag, Wiesbaden, Germany (2007).

24. K. SHAHBAZI, "An Explicit Expression for the Penalty Parameter of the Interior Penalty Method," *J. Comput. Phys.*, **205**, *2*, 401 (2005).

25. M. L. ADAMS and T. A. WAREING, "Diffusion-Synthetic Acceleration Given Anisotropic Scattering, General Quadratures, and Multidimensions," *Trans. Am. Nucl. Soc.*, **68**, 203 (1993).

26. Y. Y. AZMY, "Unconditionally Stable and Robust Adjacent-Cell Diffusive Preconditioning of Weighed-Difference Particle Transport Method Is Impossible," *J. Comput. Phys.*, **182**, 213 (2002).

27. J. S. WARSA, T. A. WAREING, and J. E. MOREL, "Krylov Iterative Methods and the Degraded Effectiveness of Diffusion Synthetic Acceleration for Multidimensional S_N Calculations in Problems with Material Discontinuities," *Nucl. Sci. Eng.*, **147**, 218 (2004).

28. Y. WANG, J. C. RAGUSA, and M. DeHART, "Xuthos: A Discontinuous Galerkin Transport Solver for Newt Based on Unstructured Triangular Meshes," *Proc. Int. Conf. Physics of Reactors: Nuclear Power: A Sustainable Resource (PHYSOR 2008)*, Interlaken, Switzerland, September 14–19, 2008 (2008).

29. J. R. SHEWCHUK, "Triangle: Engineering a 2D Quality Mesh Generator and Delaunay Triangulator," *Lecture Notes in Computer Science: Applied Computational Geometry: Towards Geometric Engineering*, Vol. 1148, Springer-Verlag, Berlin (May 1996).

30. J. RAGUSA and Y. WANG, "A Two-Mesh Adaptive Mesh Refinement Technique for S_N Neutral-Particle Transport Using a Higher-Order DGFEM," *J. Comput. Appl. Math.*, **233**, 3178 (2010).